

Chromosomal instability during neurogenesis in Huntington's disease

Albert Ruzo^{1,*}, Gist F. Croft^{1,*}, Jakob J. Metzger^{1,2,*}, Szilvia Galgoczi¹, Lauren J. Gerber¹, Cecilia Pellegrini¹, Hanbin Wang, Jr¹, Maria Fenner¹, Stephanie Tse¹, Adam Marks¹, Corby Nchako¹ and Ali H. Brivanlou^{1,‡}

ABSTRACT

Huntington's disease (HD) is a fatal neurodegenerative disease caused by expansion of CAG repeats in the Huntingtin gene (*HTT*). Neither its pathogenic mechanisms nor the normal functions of HTT are well understood. To model HD in humans, we engineered a genetic allelic series of isogenic human embryonic stem cell (hESC) lines with graded increases in CAG repeat length. Neural differentiation of these lines unveiled a novel developmental HD phenotype: the appearance of giant multinucleated telencephalic neurons at an abundance directly proportional to CAG repeat length, generated by a chromosomal instability and failed cytokinesis over multiple rounds of DNA replication. We conclude that disrupted neurogenesis during development is an important, unrecognized aspect of HD pathogenesis. To address the function of normal HTT protein we generated *HTT*^{+/-} and *HTT*^{-/-} lines. Surprisingly, the same phenotype emerged in *HTT*^{-/-} but not *HTT*^{+/-} lines. We conclude that HD is a developmental disorder characterized by chromosomal instability that impairs neurogenesis, and that HD represents a genetic dominant-negative loss of function, contrary to the prevalent gain-of-toxic-function hypothesis. The consequences of developmental alterations should be considered as a new target for HD therapies.

KEY WORDS: Huntington's disease, CRISPR, Human embryonic stem cells, Disease modeling, Chromosomal instability, Neurogenesis, DNA damage and repair

INTRODUCTION

Huntington's disease (HD) is a dominant autosomal neurodegenerative disease that is caused by an increase in the number of CAG repeats, which expands a polyglutamine (polyQ) tract in the Huntingtin (HTT) protein (Ross and Tabrizi, 2011). Despite the fact that *HTT* was among the first disease-causing genes to be cloned over 20 years ago, no therapy yet exists to treat HD (Ross and Tabrizi, 2011). It is estimated that the disease affects 1 in 10,000 Americans. The discovery of any drug that can prevent or delay the onset of HD or prolong the life of patients will make a significant contribution to the HD field in particular, but also have a major impact on neurodegenerative disease treatments in general.

HTT protein is expressed continuously in all cells from the fertilized egg onward; however, the expanded polyQ mutation notably causes the degeneration of specific populations of neurons

in the brain: medium spiny neurons and cortical projection neurons (Ross and Tabrizi, 2011). Although animal models of HD, from *Drosophila* to mouse, have been useful in understanding many aspects of cellular deterioration, they have not fully resolved the disease mechanisms or provided any effective therapies. This is likely to be due in part to species-specific differences and human-specific traits, which manifest at the molecular, cellular and tissue levels. For example, the human forebrain is greatly increased in cell number and complexity, and the normal HTT CAG repeat length is expanded from 7 in rodent to ~20 in humans. In addition, we recently reported that the human *HTT* locus encodes multiple mRNA isoforms, thus generating multiple HTT proteins, some of which are present only in higher apes and humans (hominids; Ruzo et al., 2015). Thus, HD cannot be fully studied in existing non-human model systems.

Traditionally, HD pathology has been attributed to neuronal dysfunction and death occurring during adult life. However, recent reports have begun to suggest that HTT has important roles in the developing brain, indicating that HD pathogenesis might start during embryogenesis (Godin et al., 2010; HD iPSC Consortium, 2012; Lopes et al., 2016; Molero et al., 2009, 2016). As a consequence, impaired neurodevelopment would compromise neuronal homeostasis in adulthood, leading to increased cellular vulnerability to late-life stressors (Ramocki and Zoghbi, 2008). Indeed, expression of polyQ-expanded HTT uniquely during embryogenesis results in a close recapitulation of all typical biochemical and behavioral HD phenotypes in adult mice (Molero et al., 2016). Although difficult to study in humans *in vivo*, neurons differentiated *in vitro* from induced pluripotent stem cells (iPSCs) derived from HD patients display alterations in their developmental speed, electrophysiology, metabolism, cell adhesion and, ultimately, cell death, consistent with an impairment during human neurogenesis (HD iPSC Consortium, 2012, 2017). Nevertheless, whether the polyQ-expansion constitutes a gain or a loss of normal HTT functions is still a matter of debate. Historically, aggregates of either full-length or N-terminal fragments of mutant HTT have been considered the leading cause of HD pathogenesis (Zuccato et al., 2010), although there are no studies comparing the phenotypes of polyQ-expanded versus *HTT* knockout human cells that could help properly dissect these mechanisms. While polyQ-expanded mouse embryonic stem cells (mESCs) differentiate normally to neural plate stage, mESCs deficient for HTT were unable to generate neural rosettes, demonstrating that, at least for this particular phenotype and species (mouse), mutant HTT is acting through a gain-of-function mechanism (Lo Sardo et al., 2012). Contrary to that hypothesis, a recent report using shRNA-mediated downregulation or exogenous overexpression of mutant HTT hinted that some HD phenotypes, such as a misregulation of the mitotic spindle angle in neural stem cells, may indeed be caused by a loss of HTT functions in a dominant-negative manner (Lopes et al., 2016).

¹Laboratory of Stem Cell Biology and Molecular Embryology, The Rockefeller University, New York, NY 10065, USA. ²Center for Studies in Physics and Biology, The Rockefeller University, New York, NY 10065, USA.

*These authors contributed equally to this work

‡Author for correspondence (brivanlou@rockefeller.edu)

© A.H.B., 0000-0002-1761-280X

In order to fully untangle the molecular mechanisms of HD pathology in humans, more precise tools are needed, avoiding the use of exogenous gene expression modulators (shRNAs or plasmid transfections) or lines with different genetic backgrounds that might confound the conclusions.

Here we report the generation of the first collection of isogenic human embryonic stem cells (hESCs) modeling HD as a classical genetic allelic series. Since disease onset and severity are directly proportional to polyQ length, we used CRISPR/Cas9 genome editing to engineer hESC lines that are genetically identical except for the length of the polyQ expansion. We found that these HD-hESCs recapitulate some previously reported neuronal phenotypes, thus validating the model. Importantly, they revealed an unexpected, new phenotype. Chromosomal instability during forebrain neurogenesis resulted in the generation of multinucleated neural progenitors and neurons, at a frequency proportional to polyQ length. These novel findings support the idea that HD is not just an adult-onset disease, but also a neurodevelopmental disorder. In addition, we found that these HD phenotypes were similar to those of *HTT*^{-/-}, but not *HTT*^{+/-}, hESCs, thus assigning a new function for wild-type HTT during neurodevelopment and demonstrating that HD pathology begins far earlier than expected as a dominant-negative loss-of-function, rather than through the broadly accepted gain-of-toxic-function mechanism. Collectively, these findings generate a new model for early HD pathology in which disrupted forebrain neurogenesis renders brain circuits specifically vulnerable to subsequent effects of mutant HTT or lifetime stressors. Finally, our results validate the utility of this novel HD toolkit, and we predict that it will enable the HD research community to explore further aspects of HD in other cell types and at other time points with unprecedented genetic power.

RESULTS

Generation of an HD allelic series in hESCs

In order to precisely model the correlation between polyQ length and disease severity, and elucidate the embryonic function of wild-type HTT, we combined CRISPR/Cas9 technology (Cong et al., 2013; Jinek et al., 2012; Mali et al., 2013) with ePiggyBac transposition (Lacoste et al., 2009) to edit the genome of the RUES2 hESC line [NIH0013 (James et al., 2006; Rosa et al., 2009)]. Five different polyQ lengths (45, 50, 58, 67 and 74 Q) were introduced into one of the two alleles to generate genotypes RUES2-45Q, RUES2-50Q, RUES2-58Q, RUES2-67Q and RUES2-74Q in order to model the spectrum found in HD patients, including two extreme lengths (67 and 74 Q) that cause juvenile-onset HD (Andrew et al., 1993; Duyao et al., 1993). To ensure that our gene-editing process itself did not influence any readout, we used the same approach to reinsert the normal 22Q repeat, thus creating a sixth isogenic line by regenerating wild-type RUES2, i.e. RUES2-22Q (Fig. 1A, Fig. S1A,B). To address the embryonic function of HTT we also used CRISPR/Cas9 to delete *HTT* exon 1, generating heterozygous (RUES2-*HTT*^{+/-}) and homozygous null (RUES2-*HTT*^{-/-}) *HTT* mutants (Fig. 1A, Fig. S1C-E).

Two to three independent pluripotent hESC clones were thoroughly characterized for each genotype. First, their *HTT* alleles were sequenced to confirm correct targeting and correct sequence of the non-targeted allele (Fig. S1B). Western blot confirmed expression of the appropriate wild-type and expanded full-length HTT protein, or its absence in *HTT*^{-/-} lines. There was a slight variation in overall full-length HTT expression level between lines, but without association to genotype, except for *HTT*^{+/-} lines, which showed ~60% of normal level (Fig. S1D,F). Importantly, in

lines with a polyQ expansion, there was equivalent expression from each allele (Fig. S4D-F). Immunofluorescence further confirmed the lack of full-length HTT protein in *HTT*^{-/-} lines and the reduced expression in *HTT*^{+/-} lines, and showed pan-cytoplasmic non-nuclear subcellular distribution, which was unaffected by polyQ length (Fig. 1B, Fig. S1G). All lines were validated for the absence of off-target effects in the top five predicted off-target loci (data not shown). In addition, we performed whole-genome sequencing of the core set of lines (22Q, 50Q, 58Q, *HTT*^{+/-} and *HTT*^{-/-}; data available at rues.rockefeller.edu), and demonstrated that no mutations in any of the CRISPR/Cas9 predicted off-target loci or any consistent modifications of the genome were generated by the gene-editing procedure (Table S1). Karyotype and the ability of the cells to self-renew or maintain pluripotency were unaffected (Fig. S2A,B, data not shown). Additionally, since karyotype and whole-genome sequencing analysis cannot detect copy number variation (CNV), we also screened all lines using array comparative genomic hybridization (aCGH). This demonstrated that neither CAG expansion nor loss of HTT affects the basic properties of embryonic stem cells. This collection of isogenic HD-hESC lines therefore constitutes a unique genetic toolkit that allows, for the first time, a comparison of molecular and cellular differences that are specifically due to graduated HD mutation or knockout to be made, with minimal background variability, directly in human pluripotent cells, which can differentiate to all human cell types.

HD and *HTT*^{-/-} hESCs show dysregulation of neural plate mitotic spindle orientation

Since HD is characterized by the selective degeneration of several categories of forebrain neurons, we first used the allelic series to ask whether HTT mutations, both for the CAG expanded collection, as well as for loss of HTT function, had any effect on early neural development. The formation of the nervous system begins by neural induction, which occurs by an evolutionarily conserved ‘default mechanism’ that involves inhibition of both the SMAD1/3/5 and SMAD2/3 branches of TGFβ signaling during early embryogenesis (Muñoz-Sanjuán and Brivanlou, 2002). This dual SMAD inhibition can be accomplished by exposing pluripotent embryonic cells, such as hESCs, to two small compound inhibitors: SB-431542 and LDN-193189. This inhibition leads to a direct fate conversion of hESCs after a few days of culture, from pluripotency to neuronal fates of anterior telencephalic character, and the emergence of rosette-like structures after 14 days. At day 19 after default neural induction, all isogenic lines generated typical neural rosettes (Fig. 1C,D, Fig. S2A), with no significant difference in morphology or in the expression of pan-neural [PAX6, SOX1 and nestin (NES)] or telencephalic-specific (FOXG1) markers (Fig. S2B). HTT protein was still localized in the cytoplasm of the neural progenitors at this stage, regardless of polyQ length (Fig. S2B), and appeared to be relatively enriched in the apical cytoplasm surrounding the rosette lumen. We concluded that expansion of polyQ or lack of HTT does not interfere with the initial stages of neural differentiation or positional identity in human cells. The fact that *HTT*^{-/-} hESCs could undergo neural induction and self-organize into rosettes contrasts with the observation made in *Htt*^{-/-} mESCs, and thus might represent a species-specific difference (Lo Sardo et al., 2012).

Our previous study and those of others have demonstrated a link between HTT, cell polarity and cell division in animal models (Godin and Humbert, 2011; Godin et al., 2010; Harembak et al., 2015). Since rosettes are composed of highly polarized neuroepithelial cells, with centrosomes and apical membrane

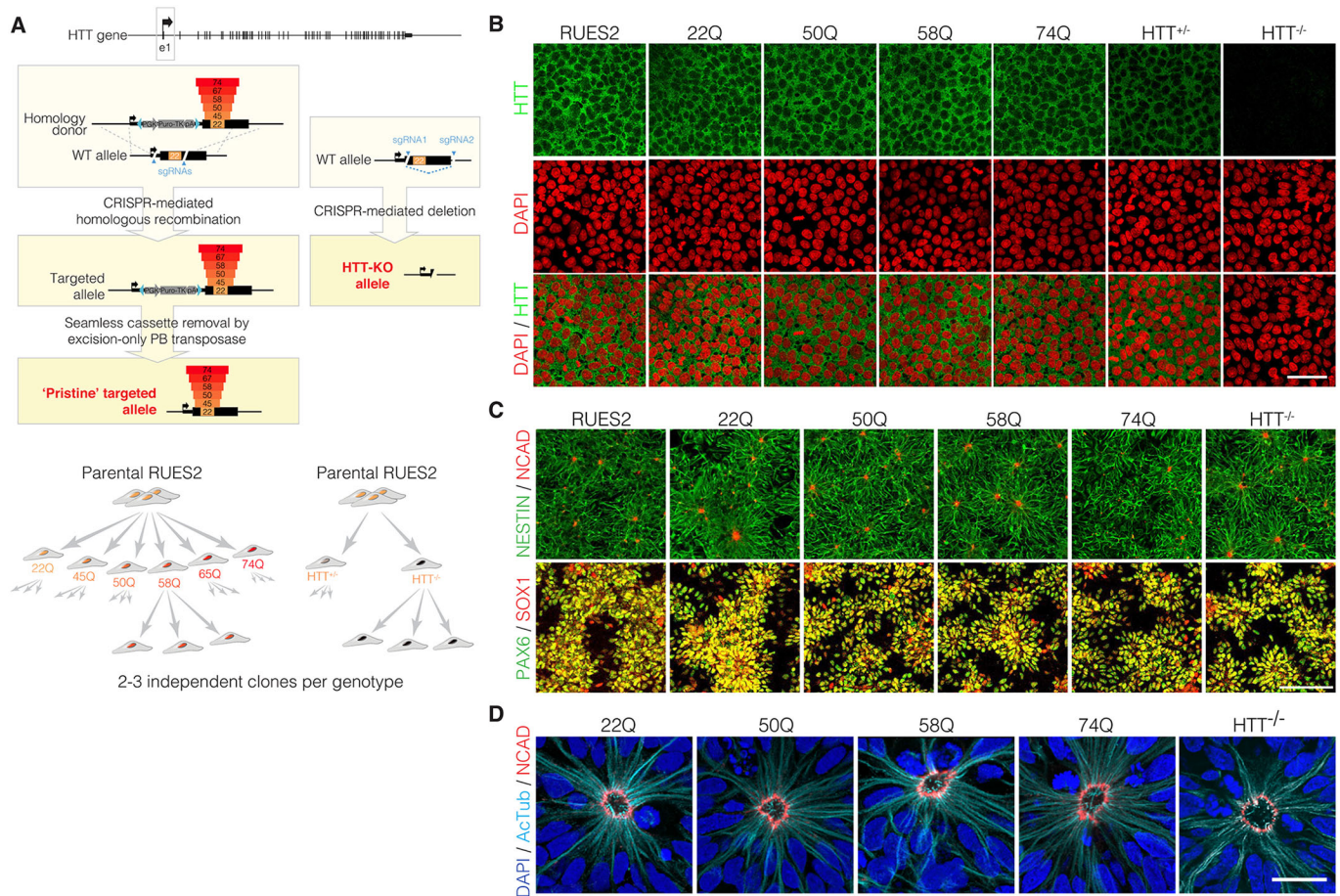


Fig. 1. Generation and validation of isogenic HD model hESC lines. (A) (Left) Strategy for generating the isogenic HD model hESC cell lines. CRISPR/Cas9-targeted homologous recombination generated hESC clones with increasing lengths of the CAG repeat region in exon 1 of the *HTT* gene, and a selection cassette flanked by ePiggyBac (ePB) terminal repeats. The ePB selection cassette was subsequently removed by transfecting an excision-only piggyBac transposase plasmid, which regenerated a 'pristine' polyQ-expanded allele. (Right) Strategy used for generating $HTT^{+/-}$ and $HTT^{-/-}$ RUES2 hESCs. A pair of sgRNAs was used to specifically delete exon 1 of the *HTT* gene. Two to three independent clones of each polyQ length and *HTT* dosage were isolated, screened for quality control, then subjected to default neural differentiation by SB-431542 plus LDN-193189 to rosette stage forebrain neuroepithelia (day 19) and lower cortical layer neurons (day 45) to search for polyQ length-dependent phenotypes. (B) Immunostaining for HTT protein (D7F7 antibody, green) and DNA staining (DAPI, red) shows that HTT is localized to the cytoplasm in hESCs and its intracellular localization is unaffected by the increasing polyQ lengths. The lack of HTT signal in $HTT^{-/-}$ clones validates the efficiency of *HTT* knockout. (C) Clones of all polyQ lengths and *HTT* dosages were able to differentiate to neural rosettes. Immunostaining of day 19 cultures showed uniform expression of neuroepithelial protein markers. (Top) Intermediate filament NES (green), and apical protein N-cadherin (red) identifying neural tube-like lumens. (Bottom) Pan-neural transcription factors PAX6 (green) and SOX1 (red) in the nuclei. (D) Clones of all polyQ lengths generated similarly organized neural rosettes. High-resolution images of individual neural rosettes, immunostained for the lumen marker N-cadherin (red), the cilia and cytoskeleton marker acetylated tubulin (cyan), and with DAPI (blue). Scale bars: 50 μ m in B; 100 μ m in C; 5 μ m in D.

proteins clustered to form a neural tube-like apical lumen, we first asked whether the size of the rosette lumen was affected by *HTT* genotype. At day 19 we found no significant difference between genotypes in the mean or population distribution of lumen areas; however, when cultures were maintained for an additional 7 days and lumen sizes increased, polyQ-expanded and $HTT^{-/-}$ lines showed a significantly reduced fraction of larger rosettes compared with the control (Fig. 2A). To address the mechanism underlying this difference, we first examined cell division polarity. As in the developing brain, nuclei undergo interkinetic nuclear migration and move to the apical pole for cell division, which then occurs adjacent to the rosette lumen, which is the *in vitro* manifestation of the neural tube. Early neuroepithelial cell divisions are symmetrical (Bayer and Altman, 2007) and occur with an orthogonal mitotic plane with respect to the lumen (Fig. 2B). Wild-type and $HTT^{+/-}$ lines showed predominantly orthogonal cell divisions as expected, whereas polyQ-expanded

and $HTT^{-/-}$ lines exhibited randomized mitotic angles, suggesting dysregulation of mitotic spindle orientation (Fig. 2C). A decrease in regulated, symmetrical divisions provides an explanation for the failure of the mutant and knockout rosettes to expand at pace with controls (Fig. 2A). In agreement with this mitotic dysregulation, both expanded polyQ and $HTT^{-/-}$ lines displayed occasional multipolar metaphase figures (Fig. 2D) and cells with supernumerary centrosomes (Fig. 2E). Our data support previous studies in mouse models and human fibroblasts (Keryer et al., 2011; Molina-Calavita et al., 2014; Sathasivam et al., 2001) and additionally suggest that mitotic angle defects and centrosomal dysregulation occur at the earliest stages of human neurodevelopment, even with physiological levels of HTT protein and common polyQ tract lengths. Finally, since the expanded polyQ HD mutants phenocopied the $HTT^{-/-}$, but not the $HTT^{+/-}$ lines, we conclude that, at least in this developmental context, HD mutations represent a loss of function.

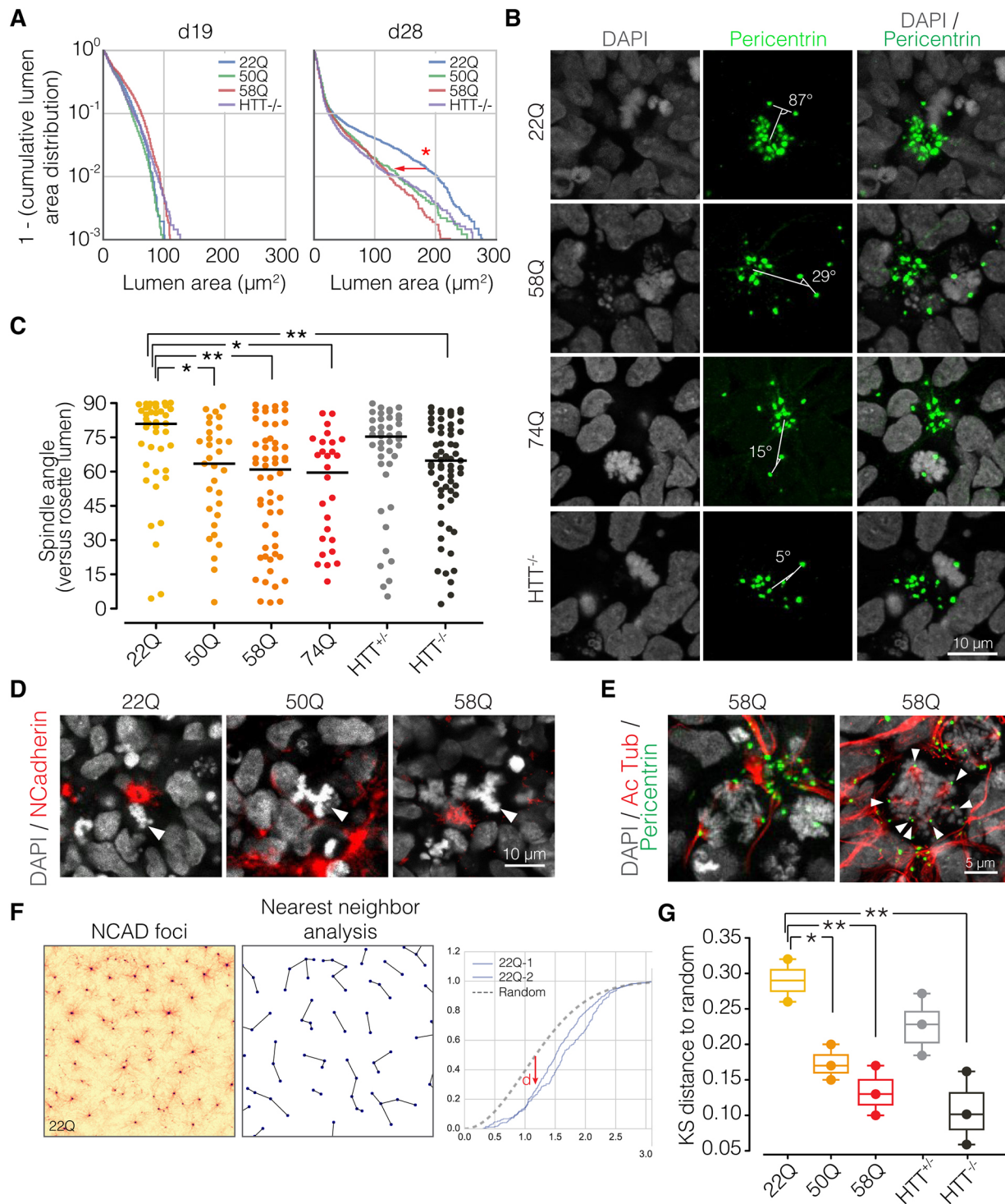


Fig. 2. HD mutations drive early neural rosette phenotypes. (A) Inverted cumulative percentage plot of rosette lumen size shows no difference between genotypes at day 19 of differentiation (5 days after reseeding), but that lumens evolve to be substantially smaller in polyQ-expanded lines and $\text{HTT}^{-/-}$ by day 28 (14 days after seeding). $n=2-3$ lines/genotype. Arrow indicates statistical comparison (* $P < 0.05$). (B) Expanded polyQ and $\text{HTT}^{-/-}$, but not $\text{HTT}^{+/+}$, lines exhibited a randomization of the angle of the mitotic plane, as compared with wild-type controls that are typically orthogonal. Immunostaining for centrosomes (pericentrin, green) and DNA staining (DAPI, white). (C) Quantification of mitotic plane angles relative to the center of the rosette lumen. Individual data points and median are shown. * $P < 0.05$, ** $P < 0.01$, Kruskal–Wallis test with Dunn’s multiple comparison post-test. Moreover, both a linear regression and a non-parametric test for trend (Jonckheere–Terpstra test) showed a significant correlation of polyQ length with the magnitude of spindle angle dysregulation ($P=2.2 \times 10^{-4}$ and $P=1 \times 10^{-4}$, respectively). (D,E) Expanded polyQ clones exhibited defects in mitosis, including (D) multipolar mitoses (arrowheads) and (E) supernumerary centrosomes (arrowheads). Staining for DNA (DAPI, white) and immunostaining for centrosomes (pericentrin, green) and acetylated tubulin (red). (F,G) Analysis of inter-rosette self-organization. (F) The distribution of nearest-neighbor distances between neural rosette lumens (N-cadherin foci) is significantly different (arrow, d) compared with a random distribution in wild-type cultures, demonstrating high-level inter-rosette self-organization. (G) Expanded polyQ and $\text{HTT}^{-/-}$, but not $\text{HTT}^{+/+}$, lines show a significantly more random spatial distribution of rosettes compared with control. $n=2-3$ lines/genotype. * $P < 0.05$, ** $P < 0.01$, ANOVA. Scale bars: 10 μm in B,D; 5 μm in E.

Neural rosette spatial self-organization is impaired in HD and *HTT*^{-/-} hESCs

We next theorized that the mitotic spindle dysregulation might impact the global spatial organization of neural rosettes, and therefore analyzed their higher order self-organization. Interestingly, rosettes in control lines displayed a highly regular organization, in which the nearest-neighbor distance distribution differed significantly from random (Fig. 2F). This demonstrates, for the first time, that cultured neural rosettes have an intrinsic, quantifiable ability to self-organize in space. Surprisingly, neural rosettes from expanded polyQ and *HTT*^{-/-} lines showed significantly diminished self-organization (Fig. 2F,G, Fig. S2C,D). *HTT*^{+/-} lines were not significantly different from control, but showed an intermediate level of organization, suggesting potential sensitivity to *HTT* gene dosage at this developmental stage. We thus concluded that HTT regulates global morphogenetic self-organization during early neural development, thus identifying a novel early function in self-organization during embryonic development. These results also suggest that HD mutations affect the earliest stages of human neurodevelopment, rather than acting primarily in adulthood, as commonly assumed.

Appearance of aberrant multinucleated neurons and progenitors during neurogenesis in HD and *HTT*^{-/-} hESCs

We next examined the extent to which our *HTT* alleles affect neurogenesis downstream of neural induction, when neuroepithelial cells transition to radial glia and their mitoses begin to produce postmitotic neurons or intermediate progenitors (Shi et al., 2012). At day 45 of *in vitro* neural differentiation, we detected no significant difference between control and mutant genotypes in the abundance of neural progenitors (SOX2⁺, NES⁺) or postmitotic neurons (CTIP2⁺, MAP2⁺) (Fig. 3A, Fig. S3A,B). Surprisingly, we detected a number of dramatic, abnormal cellular phenotypes in both progenitors and postmitotic neurons from polyQ-expanded and *HTT*^{-/-} as compared with control or *HTT*^{+/-} genotypes (Fig. 3). First, progenitor cells (NES^{high} MAP2^{low}) displayed enlarged cell somas, with multiple nuclei, disorganized filaments, and vacuoles (Fig. 3B,C, Movies 1,2). Second, neurons (MAP2^{high} NES^{low}) were seen with multiple nuclei tethered by strands of DNA into bouquet shapes, and multiple concentrically located centrosomes (Fig. 3B, D, Movie 3). Cells from polyQ-expanded and *HTT*^{-/-} lines with bouquet nuclei or large oblong nuclei showed multiple centrosomes and severe aneuploidy (Fig. 3D, Fig. 4D, Movie 4). The frequency of these abnormal phenotypes in polyQ-expanded or *HTT*^{-/-} was higher than in control or *HTT*^{+/-} genotypes, and displayed a statistically significant correlation to the length of the polyQ expansion ($P=0.013$ in a linear regression model and $P=0.012$ in the Jonckheere–Terpstra non-parametric trend test). As in the rosette phenotypes, *HTT*^{+/-} lines showed a mild phenotype (Fig. 3E, Fig. S3C). These data are again consistent with a dominant-negative loss-of-function model for this aspect of HD. Collectively, these cellular phenotypes are characteristic of chromosomal instability, which can result from defects in many aspects of the mitotic apparatus or unresolved DNA damage.

Chromosomal instability was not observed during pluripotency in any of our lines, suggesting that this is a time-specific event. During pluripotency, HTT protein(s) were selectively localized in the cytoplasm and excluded from the nucleus before or during cell divisions. We therefore evaluated the levels and subcellular localization of HTT proteins by western blot and immunofluorescence in neural progenitors and neurons. Western blot analysis established that HTT protein expression was increased from pluripotency to day-22 neural rosettes, and subsequently

decreased at day 40 during neurogenesis (Fig. S4D). We note that the stoichiometric ratio of wild-type HTT to expanded CAG HTT remains unchanged from pluripotency (Fig. S1F) to the last time point of neurogenesis (day 40, Fig. S4D,E). Immunofluorescence revealed several differences in HTT protein distribution. First, in postmitotic neurons (MAP2⁺ CTIP2⁺) HTT protein was detected in both the cytoplasm and, in contrast to pluripotent cells, in the nucleus (Fig. 3F, top). In progenitor cells (SOX2⁺ NES⁺), HTT was more enriched and punctate in the apical perinuclear cytoplasm (Fig. 3F, *HTT*^{+/-}). HTT also showed a stereotypical subcellular localization during mitosis: enriched at both apical poles as well as the midplane at anaphase (Fig. 3F, *HTT*^{+/-}, arrowhead). In polyQ-expanded lines the HTT signal was greatly increased in the abnormal multinucleated cells, displaying large, bright puncta suggestive of aggregates, both in the cytoplasm and the nuclei, with a particularly dense enrichment at the multicentrosomal location described above (Fig. 3F, 45Q and 74Q, arrows).

Both polyQ expansion and loss of HTT lead to chromosomal instability

To determine the mechanisms for the emergence of aberrant neurons, we first asked if multinucleation arose from cell fusion or dysregulated cell division. Time-lapse imaging of mixed RFP-labeled and GFP-labeled cultures showed no cell fusion events in any genotype (data not shown). However, whereas control clones exhibited normal cell cycle progression (Movie 5), polyQ-expanded and *HTT*^{-/-} lines displayed failed cytokinesis over multiple rounds of karyokinesis (Fig. 4A, Movies 6,7). These unsuccessful divisions usually failed at the terminal separation of daughter cells (abscission). Failed abscission can result from defects in the assembly of the telophase midbody, but we found that the key abscission proteins citron kinase and aurora B kinase constituted normal midbodies in all genotypes (Fig. 4B, data not shown). However, polyQ-expanded and *HTT*^{-/-} anaphases and telophases showed lagging chromosomes and chromatin bridges, respectively (Fig. 4B), which are known to lead to abscission failure if unresolved by DNA repair proteins (Steigemann et al., 2009). Importantly, we detected lagging chromosomes even in the context of normal ploidy (Fig. 4C, Movie 8), whereas all multinucleated cells with DNA strands had high levels of aneuploidy (Fig. 4D). These findings further support the hypothesis that both HD polyQ-expansion mutations and the loss of HTT can lead to chromosomal instability. Furthermore, they suggest that HTT normally prevents DNA damage, and loss of this function leads to the chromosomal instability phenotypes that we describe.

DISCUSSION

A novel genetic toolkit

We have created a novel genetic toolkit in hESCs that, for the first time, allows the comparison of molecular and cellular differences that are specifically due to either graduated HD mutation or to *HTT* knockout. Using CRISPR/Cas9 gene-editing technology we generated a series of lines with different CAG lengths, with minimal genetic background variability. Because these cells are of human origin, and are based on a precisely edited endogenous *HTT* locus, they offer significant advantages over previous cell models in other species and other expression systems, as our lines maintain endogenous regulation of gene dosage and contain common, clinically significant CAG lengths. Because they are pluripotent they provide the means to access all human cell types at all developmental stages, including specific neural lineages classically known to be affected in HD. We have validated our allelic series as an HD model by confirming previous reports of mitotic angle

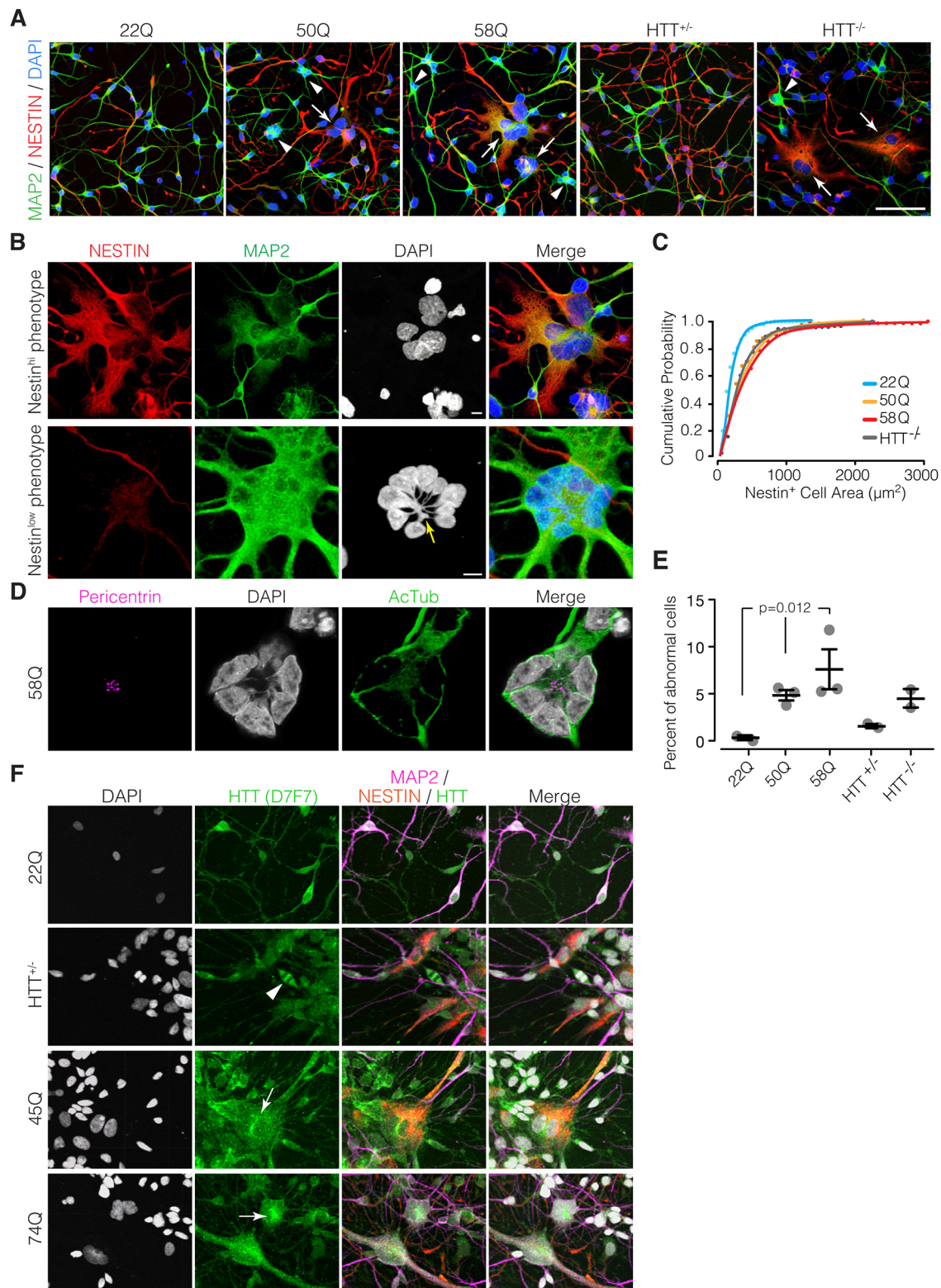


Fig. 3. See next page for legend.

dysregulation in polyQ-expanded and $HTT^{-/-}$ forebrain neural progenitor cells, and have further demonstrated its unique power by providing entirely novel insight into HTT function and HD pathology during early neural development. We believe that this new allelic series will become a valuable resource for studying HTT and HD biology in many specific cell types and developmental

stages, in a human genetic, molecular and cellular background. In the future, it will also be of extreme interest for the HD community to expand this HD allelic series to other hESC lines. This will allow comparison between different genders and genetic backgrounds, to assess the possibility that some phenotypes are particularly enhanced in a specific genetic background.

Fig. 3. Expanded polyQ and *HTT*^{-/-} lines show abnormal cellular phenotypes in early neurogenesis phase. (A) Immunofluorescence for progenitors (NES, red), neurons (MAP2, green) and DNA staining (DAPI, blue) identifies two mutant cellular phenotypes in expanded polyQ and *HTT*^{-/-} clones: large progenitor cells (arrows) with large soma, multiple nuclei, disorganized filaments and vacuoles; and neurons with multiple nuclei (arrowheads). 3D rendering of 40× confocal z-stacks. (B) Higher resolution (100× confocal image, Imaris 3D rendering) of (top) an aberrant progenitor cell (NES^{high} MAP2^{low}) from the RUES2-58Q line, showing multinucleation, vacuolation and filament disorganization; and (bottom) an aberrant postmitotic neuron (NES^{low} MAP2^{high}) from the RUES2-50Q line, with a typical nuclear bouquet structure (yellow arrow). (C) Expanded polyQ and *HTT*^{-/-} lines display an increase in larger NES^{high} cells. Shown is a cumulative probability curve of NES⁺ cell areas, the sum of two to three lines/genotype. (D) Aberrant polarization of abnormal postmitotic neurons. Centrosomes (pericentrin, magenta) are located in the center of the soma, surrounded by subnuclei (100× confocal z-section). DAPI, gray. (E) Quantification of the frequency of aberrant cells, showing mean±s.e.m. percentage of cells with abnormally large cell soma among all DAPI-stained cells; *n*=2-3 lines/genotype. Both a linear regression and a non-parametric test for trend (Jonckheere–Terpstra test) showed significant correlation between the length of the polyQ expansion and the abundance of multinucleated cells (*P*=0.013 and *P*=0.012, respectively). (F) Unlike in pluripotency and at early neural rosette stage, immunofluorescence of HTT (D7F7 antibody, green) in postmitotic neurons shows a granular, but uniform, signal in nucleus and cytoplasm (22Q). In polyQ-expanded multinucleated neurons and progenitors, the HTT signal accumulates in bright puncta, in the nuclear cleft region where multicentrosome clusters are located (45Q and 74Q, arrows). Interestingly, in mitotic figures at this stage, HTT was enriched at spindle poles and in between the separating chromosomes during anaphase (*HTT*^{+/-}, arrowhead). Scale bars: 40 µm in A; 5 µm in B.

HD has a developmental origin

We present new evidence for a strong developmental component of HD. Little attention has traditionally focused on embryonic development in HD; however, our data support and expand on a growing body of literature that has begun to define important effects at multiple stages of neurodevelopment (Barnat et al., 2017; Molero et al., 2009, 2016; Molina-Calavita et al., 2014; Nopoulos et al., 2011; White et al., 1997). Notably, a study of mouse forebrain neurogenesis reported a series of phenotypes remarkably similar to those we describe *in vitro*, including an increased volume of progenitor cells, and irregular, fused, misshapen nuclei (Molero et al., 2009). Our findings now suggest that chromosomal instability is a key cellular mechanism underpinning these phenotypes, and future studies in HD mice should test this possibility directly. Another study provided perhaps the most convincing genetic evidence of key pathological events during development by demonstrating that conditional expression of mutant HTT in mice during development alone reproduces the near-complete adult-onset HD phenotypes (Molero et al., 2016). Our data shed light on the molecular mechanism behind these phenotypes in a human neural developmental context, and support the contention that HD is indeed a developmental disease.

Our results suggest that the chromosomal instability phenotype displays cell type and developmental stage specificity, since it is not present during pluripotency or early neuronal induction, but only when progenitor cells initiate neurogenesis. It will be important to exploit this specificity in future work to determine what makes these cells specifically dependent on HTT function. The answer might point to an evolutionary function for HTT in the enlargement and diversification of the human forebrain, which was accomplished in large part by an increasing diversification of progenitor cell types and modes of division, ultimately expanding both the total number and diversity of neurons (Namba and Huttner, 2017). Furthermore, this presents an opportunity to test whether this mechanism might

be responsible for the selective vulnerability of cortical and medium spiny neurons in HD. Both are forebrain CTIP2⁺ cell types, and thus it will be important to determine if chromosomal instability affects the ventral and dorsal forebrain CTIP2⁺ lineage in a similar manner.

Cause of chromosomal instability

Chromosomal instability can result from a variety of organelle and molecular defects, including those affecting chromosome positioning during anaphase (via defects in microtubules), motor proteins, kinetochores or centrosomes, which could be related to mitotic spindle angle regulation as previously suggested in HD (Elias et al., 2014; Haremakei et al., 2015; Lopes et al., 2016; Molina-Calavita et al., 2014). However, the chromosomal instability that we describe, especially given the observation of lagging DNA in the context of normal centrosome and spindle organization, suggests that one of the primary defects could be increased DNA damage or dysfunctional DNA replication/repair, which would lead to entangled or dicentric chromosomes. Several lines of evidence support this DNA damage/repair model. First, recent genome-wide association studies identified DNA repair genes, such as *FANL*, as the main genetic modifiers that significantly accelerate or delay the age of disease onset regardless of CAG length (GeM-HD Consortium, 2015; Jones et al., 2017; Lu et al., 2014). Indeed, increased baseline chromosomal instability might provide a new explanation for the significantly reduced incidence of cancer in HD patients (Sørensen et al., 1999), since it typically leads to apoptotic elimination of pre-cancerous cells in the early stages of transformation (Funk et al., 2016). These findings support our implication that DNA damage/repair is a more likely primary cause for these novel chromosomal instability neurodevelopmental alterations, but future work will test this hypothesis.

Integration with previous reports and models

Our conclusions are consistent with, and expand, previous observations made in human HD-iPSCs and other HD models. These include the detection of abnormal nuclear morphology (Nekrasov et al., 2016) and early neural rosette phenotypes where differences in adhesion with long CAG expansions was observed (HD iPSC Consortium, 2012). Additionally, our observations are also consistent with a role of HTT in nuclear pore function, as seen in neurons from HD mice, human iPSCs and human HD brain samples, where misshapen nuclei, HTT aggregates, and increased double-stranded breaks were also observed (Gasset-Rosa et al., 2017; Grima et al., 2017). In light of our results, it is tempting to speculate that early DNA damage during neurogenesis sets the stage for later nuclear envelope and nuclear pore defects.

Our observations on rosette organization and neurogenesis are also consistent with a role of HTT in the establishment/maintenance of polarity. Our data on rosette size and secondary organization should be considered along with reports of reduced cell adhesion in HD-iPSC neural progenitor cells, neural tube defects in zebrafish embryos, randomization of epithelial polarity in the skin of frog embryos, and reduced rosette formation in mESCs (Haremakei et al., 2015; HD iPSC Consortium, 2012; Lo Sardo et al., 2012). Of particular interest is an assessment of the possible involvement of the ADAM10/N-cadherin pathway in the phenotypes that we observe (Lo Sardo et al., 2012).

Gain- or loss-of-function and proportionality to polyQ length

Whether the HD mutation represents a gain- or loss-of-function has been the subject of debate, and remains controversial. Historically,

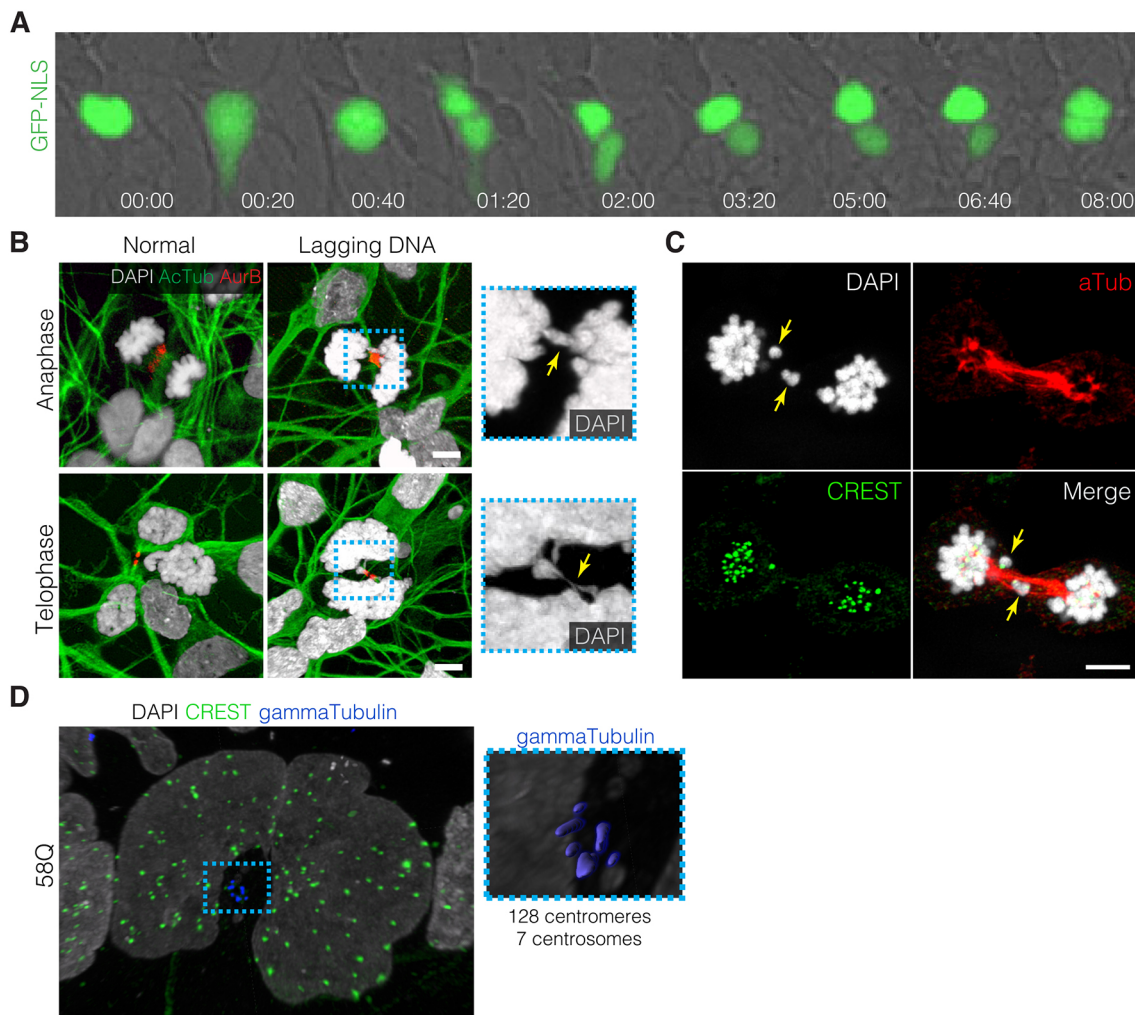


Fig. 4. Expanded polyQ and *HTT*^{-/-} neurogenesis phenotypes are caused by defects in cytokinesis. (A) Representative frames from continuous time-lapse imaging of NLS-marked nuclei (green) between days 29 and 32, showing that supernumerary nuclei are generated by nuclear replication and failed cytokinesis. Time stamp is h:min. (B) Mitotic anaphases and telophases in expanded polyQ and *HTT*^{-/-} lines show lagging DNA and chromatin bridges (insets, yellow arrows) through the cleavage furrow and midbody (marked by aurora B kinase, red). (C) A dividing cell with normal centromere counts (92) displaying lagging chromosomes in RUES2-58Q. CREST is a centromeric protein. (D) Multinucleated cells are aneuploid. Representative image of a RUES2-58Q cell with a large horseshoe-shaped nucleus containing 128 chromosomes (by centromere staining, CREST) and multiple centrosomes (gamma-tubulin). (B,C) 3D Imaris rendering of 100× confocal z-stacks; (D) a rendered 20 µm oblique virtual slice from a larger stack. Scale bars: 5 µm in B,C.

HD had been considered a toxic gain-of-function, supported initially by the fact that homozygous and heterozygous HD patients display the same age of symptom onset and clinical course, which indicates that the presence of a wild-type allele is not beneficial (Wexler et al., 1987), as well as by the fact that the embryonic lethality of *Htt* knockout in mice can be rescued by mutant HTT (Leavitt et al., 2001). On the other hand, recent evidence supports loss-of-function as being the basis of, or at least involved in, HD. These include studies of polarity and cell division in amphibian embryos, mouse mammary stem cells, and human cortical progenitor cells derived from non-isogenic hESC lines, which suggest a loss-of-function and dominant-negative effect of HD CAG expansion mutations (Elias et al., 2014; Harembaki et al., 2015; Lopes et al., 2016). These studies, however, did not have the luxury of an isogenic *HTT*^{-/-} line to directly and quantitatively compare the CAG expansion with complete loss-of-function phenotypes in human cells as we have in our study. Although we strongly believe this to be the case, the ultimate and most stringent evidence for a true dominant-negative effect requires rescue

experiments, in which the observed effects of CAG expansion and *HTT*^{-/-} can be reverted by co-expression of wild-type HTT.

One of the most tantalizing genetic questions in HD biology is the remarkably direct inverse correlation between polyQ length and disease onset (Duyao et al., 1993). We designed our platform to have the potential to finally allow a mechanistic understanding of the timing and severity of the disease. We demonstrate that both spindle orientation dysregulation and multinucleated cell generation increased with CAG length. However, it is possible, even likely, that HTT has multiple functions at multiple developmental stages and in different cell types, and thus that the overall clinical phenotype might be a combination of multiple molecular or cellular phenotypes. Finally, while a dominant-negative loss-of-function model does not necessarily require polyQ length proportionality (Lopes et al., 2016), we note that there is a linear relationship with our observed phenotypes.

Implications for clinical aspects of HD

How could these new discoveries based on isogenic HD-hESC lines contribute to an understanding of HD pathology and to bringing

patients one step closer to a much-needed therapy? It is tempting to speculate that the multinucleated neuronal progenitors are destined to undergo cell death, and gradually over decades. This hypothesis is in agreement with the phenotype of the citron kinase knockout mouse, where cortical neurons show nuclear bouquets and multiple centromeres, phenocopying our neuronal phenotype. In these mice, multinucleated cortical neurons are gradually eliminated by apoptosis (Anastas et al., 2011; Mitchell et al., 2001). If this were the case in human HD, the total cortical neuron pool would gradually diminish, therefore enhancing vulnerability to accumulated homeostatic burdens of age. Additionally, dying cells might leave scarring or residual inflammation. Another possibility is that surviving multinucleated HD neurons might integrate into circuits, perturbing their normal function and eventually leading to degeneration.

Most fundamentally, our findings collectively argue that the consequences of early defects must be considered when developing therapies for HD, even when symptoms only appear decades later.

MATERIALS AND METHODS

Generation of an isogenic set of HD model hESC lines

In order to establish an optimal platform for understanding the effects of HD mutations, we used CRISPR/Cas9 technology to generate a set of isogenic hESC lines that would differ only in the *HTT* locus, bearing different lengths of the CAG tract. The already established, registered and validated RUES2 hESC line (NIH hESC-09-0013) was used as the parental line. Genetic analysis of the *HTT* gene in RUES2 showed that it contained 20 and 22 CAGs. The homology donors for the CRISPR/Cas9-mediated homologous recombination were designed to contain ~1 kb homology arms flanking *HTT* exon 1, a piggyBac transposable element containing a Puro-TK cassette (for both negative and positive selections), and various versions of *HTT* exon 1 containing different lengths of the CAG tract (20, 42, 48, 56, 67, 72 CAGs). To construct the homology donors, we first generated a parental plasmid using Gibson assembly, in which we could easily swap the length of the CAG tract. All fragments needed for the assembly were amplified using Q5 high-fidelity polymerase (NEB) or the GC-RICH PCR System (Sigma-Aldrich) using the primers listed in Table S3.

This resulting 'base' homology donor plasmid contained a 20 CAG repeat tract, which could easily be swapped using the flanking *XmnI* and *BbsI* sites. To create the homology donor plasmids with expanded CAG lengths, we PCR amplified the *HTT* exon 1 region from genomic DNAs obtained from iPSCs or fibroblasts derived from HD patients, and cloned them into the 'base' plasmid using *XmnI* and *BbsI*. The primers used for the CAG tract amplification were polyCAG_Fw CCAAGATGGACGGCCGCTC and polyCAG_Rv AGGACAAGGGAAGACCCAAG. The origin of the templates used for each CAG length are summarized in Table S4.

For the CRISPR/Cas9-mediated targeting, multiple sgRNAs were designed to recognize sequences near the CAG tract, but gene targeting attempts using a single sgRNA were unsuccessful. However, an optimized strategy that combined two sgRNAs targeting sequences that flanked the CAG tract proved to be much more efficient in generating the desired homologous recombination: hHTT_sgRNA25 and hHTT_sgRNA14 (Table S5). These two sgRNAs were cloned into a Cas9 nickase expression vector (pX335 from the Feng Zhang lab, Addgene plasmid #42335). Both CRISPR plasmids, together with the appropriate homology donor, were nucleofected into RUES2 cells using a Nucleofector II instrument and Cell Line Nucleofector Kit L (Lonza). Puromycin was added to the cultures 5 days after nucleofection, and kept in for 5 more days to ensure selection of correctly targeted clones. Puromycin-resistant cells were then nucleofected with an excision-only piggyBac transposase (Transposagen), and a subsequent ganciclovir treatment selected clones in which the selection cassette had been correctly removed, leaving a minimal footprint (one extra nucleotide in the 5'UTR). Colonies derived from single cells were picked and expanded for screening. PCR amplification and Sanger sequencing identified correctly targeted clones, with no mutations in the CRISPR/Cas9 target sites or the piggyBac excision site. All positive clones were heterozygously targeted, which is a common finding in long genetic insertions via CRISPR/Cas9-

mediated homologous recombination, and there appeared to be no preference as to which allele had been targeted. We selected two to three independent clones for each CAG length to serve as independent biological replicates. Normal HTT expression was confirmed by western blot, and all lines were karyotyped by G-banding and aCGH analyses to assess their genomic integrity and CNV. We found a variety of CNVs and loss of heterozygosity, within and outside of normal ranges (Fig. S2C, Table S2), but these did not correlate with any of the observed phenotypic differences and were not the result of gene editing per se, as they were also present in genetically unmodified clones. Whole-genome sequencing was performed at NY Genome Center (NYGC) using the TruSeq DNA PCR-Free Kit for Library Preparation and run in an Illumina HiSeqX sequencer. Around 1000 unique single-nucleotide polymorphisms were identified in each line, probably caused by a founder effect from a genetically variable parental RUES2 cell line. The pluripotency status and absence of differentiation of the clones were validated through immunofluorescence staining of cells seeded and cultured on micropatterned coverslips (CYTOO).

Generation of isogenic *HTT*^{+/+} and *HTT*^{-/-} hESC lines

We used CRISPR/Cas9 technology to generate a set of isogenic hESC lines with different *HTT* gene dosages (*HTT*^{+/+}, *HTT*^{+/-}, *HTT*^{-/-}). RUES2 hESC (NIH hESC-09-0013) was used as the parental line. To create *HTT*^{-/-} and *HTT*^{+/-} lines, CRISPR/Cas9 was used to delete the first exon of *HTT*, ensuring that no protein fragment would be produced in the targeted ('null') allele. An optimized strategy that combined two sgRNAs that flanked the first exon proved to be efficient in generating the desired deletion: hHTT_sgRNA22 and hHTT_sgRNA14 (Table S5). These two sgRNAs were cloned into an SpCas9 expression vector (pX330 from the Feng Zhang lab), modified to coexpress a puromycin cassette to facilitate selection of transfected cells, thus maximizing the percentage of targeted colonies. Both CRISPR plasmids were nucleofected into RUES2 cells using a Nucleofector II instrument and Cell Line Nucleofector Kit L (Lonza). Puromycin was added to the cultures 24 h after nucleofection, and kept in for a further 24 h to select for transfected cells. Colonies derived from the puromycin-resistant cells were picked and expanded for screening. PCR amplification and Sanger sequencing identified correctly targeted clones with the desired exon 1 deletion. Two to three clones per genotype were identified and further validated as above.

Neural differentiation

Isogenic lines were subjected to a default neural induction protocol adapted from Shi et al. (2012). In short, cultures were seeded in suspension, or in confluent adherent culture, at 0.5–1×10⁶ cells/ml and fed every other day with N2B27 serum-free medium with ROCK inhibitor (20 μM, Abcam) for the first 2 days, TGFβ inhibition (10 μM SB-431542, Sigma and 0.2 μM LDN-193189, StemGent) for the first 10 days, treated with 5 ng/ml FGF8 (R&D Systems) from day 12–22 to maximize the frequency of CTIP2 (BCL11B)-positive cells, dissociated and seeded on adherent substrate (polyornithine/laminin, Ibidi) at day 14, fixed and analyzed at day 19 or continued in culture with added BDNF (R&D Systems) and IGF1 (R&D Systems, 10 ng/ml), cAMP (1 μM, R&D Systems) and ascorbic acid (200 μM, Sigma), until dissociation and reseeded on substrate at day 40, and fixation and analysis at day 45.

Immunostaining and imaging

Cultures were fixed with 4% paraformaldehyde (PFA), rinsed twice with PBS, and then permeabilized and quenched with wash buffer (PBS+0.1% Triton X-100) containing 100 mM glycine and 0.1% sodium azide, blocked (wash buffer, 10% normal donkey serum, 0.1% sodium azide) for 30 min, incubated with primary antibodies overnight at 4°C (for primary antibodies and dilutions, see Table S6), washed three times in wash buffer for 5 min each, incubated with secondary antibodies (Alexa 488, 555, 594, 647, Molecular Probes; 1:500) and DAPI nuclear counterstain for 1 h at room temperature, and then washed as above.

For mitotic synchronization and microtubule visualization, cultures were synchronized at G-to-M transition with nocadazole (0.2 μM; Abcam) for 18 h, then rinsed and released for 2 h, fixed for 5 min at room temperature in culture medium with 2% PFA, then incubated for 30 min at 37°C in

microtubule stabilization buffer [0.1 M PIPES pH 6.9, 5 mM MgCl₂, 2.5 mM EGTA, 2% formaldehyde, 0.1% Triton X-100, 1 μM paclitaxel (Sigma), 10 U/ml aprotinin (Sigma) and 50% deuterium oxide (Messinger and Albertini, 1991)] before quench and blocking as above. Z-stack images were acquired on a Leica SP8 inverted confocal microscope at 12 bits in 1024 pixels × 1024 pixels using an HCX PL APO CS ×20/0.75 NA air-immersion objective, an HC PL APO CS2 ×40/1.10 NA water-immersion objective, or an HC PL APO ×100/1.4 oil-immersion objective (Leica) at Nyquist spacings. Images were then deconvolved with a 3D blind algorithm (ten iterations) using AutoDeblur X software (Autoquant) and rendered in Imaris (Bitplane). 3D rendering channels were subject to uniform non-linear adjustment across the entire volume to highlight salient details; adjustments were identical across genotypes.

Analysis of neural rosette spatial distribution

Rosettes were identified by training a classifier on N-cadherin antibody stains using Ilastik (Sommer et al., 2011). N-cadherin-positive areas were thresholded in size (15 μm²) to eliminate small N-cadherin spots that were not fully developed rosettes. The quantification results were not dependent on the specific value chosen for the threshold. The nearest-neighbor distributions were obtained using the k-d tree implementation in scikit-learn (<http://scikit-learn.org>) and were compared with the random distribution using the one-sample Kolmogorov–Smirnov distance between them. The cumulative nearest-neighbor distribution F for a random set of points in two dimensions can easily be calculated as

$$F(d) = 1 - e^{-\lambda \pi d^2},$$

where λ is the 2D density of foci, and d is the distance between two neighbors. We rescaled the data for the individual lines separately according to their λ .

Time-lapse imaging

Neural cultures were dissociated to single cells at day 25, and reseeded at 0.5 × 10⁶/cm² on polyornithine laminin-coated 35 mm imaging dishes (Ibidi). One day later, cultures were transduced with GFP and RFP nucleus-labeling baculoviruses (CellLight BacMam 2.0, ThermoFisher Scientific) for 24 h. Two days later, when the nuclear signal was clearly observable, a time-lapse imaging acquisition was carried out for 3 days using a CellVoyager CV1000 spinning-disk confocal microscope (Yokogawa).

Acknowledgements

We thank the members of the A.H.B. laboratory for advice and criticism, and especially Alessia Deglincerti for early work on the allelic series; Alison North, Kaye Thomas, Tao Tong and Christina Pyrgaki of the Rockefeller University Bioimaging Research Center for superlative technical advice and support on microscopy and image analysis; Eric Siggia for constructive criticism; Hironori Funabiki for crucial scientific advice; Jean-Marx Santel for administrative assistance; Amir Brivanlou for critical reading of the manuscript; Dr Sarah Tabrizi for sharing HD patient-derived fibroblasts; and we appreciate thoughtful criticisms and comments on work at all stages of this project from CHDI, especially from Tom Vogt, Dan Felsenfeld and Ignacio Muñoz-Sanjuán.

Competing interests

The authors declare no competing or financial interests.

Author contributions

Conceptualization: A.R., G.F.C., A.H.B.; Methodology: A.R.; Software: J.J.M.; Validation: A.R.; Formal analysis: A.R., G.F.C., J.J.M.; Investigation: A.R., G.F.C., J.J.M., S.G., L.J.G., C.P., H.W., M.F., S.T., A.M., C.N.; Resources: A.R.; Data curation: A.R., G.F.C.; Writing - original draft: A.R., G.F.C.; Writing - review & editing: A.R., G.F.C., J.J.M., A.H.B.; Visualization: A.R.; Supervision: A.H.B.; Project administration: A.R., A.H.B.; Funding acquisition: A.H.B.

Funding

This work was funded by the CHDI Foundation (A-9423), New York State Stem Cell Science (NYSTEM) (C028128), RUMI Scientific, The Robertson Foundation and Rockefeller University.

Data availability

The whole-genome sequence data have been uploaded to the Sequence Read Archive at NCBI under Accession number SRP130095 or bioProject number PRJNA430518.

Supplementary information

Supplementary information available online at <http://dev.biologists.org/lookup/doi/10.1242/dev.156844.supplemental>

References

- Anastas, S. B., Mueller, D., Semple-Rowland, S. L., Breunig, J. J. and Sarkisian, M. R. (2011). Failed cytokinesis of neural progenitors in citron kinase-deficient rats leads to multiciliated neurons. *Cereb. Cortex* **21**, 338–344.
- Andrew, S. E., Goldberg, Y. P., Kremer, B., Telenius, H., Theilmann, J., Adam, S., Starr, E., Squitieri, F., Lin, B. and Kalchman, M. A. (1993). The relationship between trinucleotide (CAG) repeat length and clinical features of Huntington's disease. *Nat. Genet.* **4**, 398–403.
- Barnat, M., Le Friec, J., Benstaali, C. and Humbert, S. (2017). Huntingtin-mediated multipolar-bipolar transition of newborn cortical neurons is critical for their postnatal neuronal morphology. *Neuron* **93**, 99–114.
- Bayer, S. A. and Altman, J. (2007). *The Human Brain During the Early First Trimester*, 1st edn. Boca Raton: CRC Press.
- Cong, L., Ran, F. A., Cox, D., Lin, S., Barretto, R., Habib, N., Hsu, P. D., Wu, X., Jiang, W., Marraffini, L. A. et al. (2013). Multiplex genome engineering using CRISPR/Cas systems. *Science* **339**, 819–823.
- Duyao, M., Ambrose, C., Myers, R., Novelletto, A., Persichetti, F., Frontali, M., Folstein, S., Ross, C., Franz, M. and Abbott, M. (1993). Trinucleotide repeat length instability and age of onset in Huntington's disease. *Nat. Genet.* **4**, 387–392.
- Elias, S., Thion, M. S., Yu, H., Sousa, C. M., Lasgi, C., Morin, X. and Humbert, S. (2014). Huntingtin regulates mammary stem cell division and differentiation. *Stem Cell Reports* **2**, 491–506.
- Funk, L. C., Zasadil, L. M. and Weaver, B. A. (2016). Living in CIN: mitotic infidelity and its consequences for tumor promotion and suppression. *Dev. Cell* **39**, 638–652.
- Gasset-Rosa, F., Chillón-Marin, C., Goginashvili, A., Atwal, R. S., Artates, J. W., Tabet, R., Wheeler, V. C., Bang, A. G., Cleveland, D. W. and Lagier-Tourenne, C. (2017). Polyglutamine-expanded huntingtin exacerbates age-related disruption of nuclear integrity and nucleocytoplasmic transport. *Neuron* **94**, 48–57.e4.
- Genetic Modifiers of Huntington's Disease (GeM-HD) Consortium: Lee, J.-M., Wheeler, V. C., Chao, M. J., Vonsattel, J. P. G., Pinto, R. M., Lucette, D., Abu-Elneel, K., Ramos, E. M., Mysore, J. S., Gillis, T. et al. (2015). Identification of genetic factors that modify clinical onset of Huntington's disease. *Cell* **162**, 516–526.
- Godin, J. D. and Humbert, S. (2011). Mitotic spindle: focus on the function of huntingtin. *Int. J. Biochem. Cell Biol.* **43**, 852–856.
- Godin, J. D., Colombo, K., Molina-Calavita, M., Keryer, G., Zala, D., Charrin, B. C., Dietrich, P., Volvert, M.-L., Guillemot, F., Dragatsis, I. et al. (2010). Huntingtin is required for mitotic spindle orientation and mammalian neurogenesis. *Neuron* **67**, 392–406.
- Grima, J. C., Daigle, J. G., Arbez, N., Cunningham, K. C., Zhang, K., Ochaba, J., Geater, C., Morozko, E., Stocksdale, J., Glatzer, J. C. et al. (2017). Mutant huntingtin disrupts the nuclear pore complex. *Neuron* **94**, 93–107.e6.
- Harembak, T., Deglincerti, A. and Brivanlou, A. H. (2015). Huntingtin is required for ciliogenesis and neurogenesis during early *Xenopus* development. *Dev. Biol.* **408**, 305–315.
- HD iPSC Consortium: Mattis, V. B., Svendsen, S. P., Ebert, A., Svendsen, C. N., King, A. R., Casale, M., Winokur, S. T., Batugedara, G., Vawter, M., Donovan, P. J. et al. (2012). Induced pluripotent stem cells from patients with Huntington's disease show CAG-repeat-expansion-associated phenotypes. *Cell Stem Cell* **11**, 264–278.
- HD iPSC Consortium: Lim, R. G., Salazar, L. L., Wilton, D. K., King, A. R., Stocksdale, J. T., Sharifabad, D., Lau, A. L., Stevens, B., Reidling, J. C., Winokur, S. T. et al. (2017). Developmental alterations in Huntington's disease neural cells and pharmacological rescue in cells and mice. *Nat. Neurosci.* **20**, 648–660.
- James, D., Noggle, S. A., Swigut, T. and Brivanlou, A. H. (2006). Contribution of human embryonic stem cells to mouse blastocysts. *Dev. Biol.* **295**, 90–102.
- Jinek, M., Chylinski, K., Fonfara, I., Hauer, M., Doudna, J. A. and Charpentier, E. (2012). A programmable dual-RNA-guided DNA endonuclease in adaptive bacterial immunity. *Science* **337**, 816–821.
- Jones, L., Houlden, H. and Tabrizi, S. J. (2017). DNA repair in the trinucleotide repeat disorders. *Lancet Neurol.* **16**, 88–96.
- Keryer, G., Pineda, J. R., Liot, G., Kim, J., Dietrich, P., Benstaali, C., Smith, K., Cordelières, F. P., Spassky, N., Ferrante, R. J. et al. (2011). Ciliogenesis is regulated by a huntingtin-HAP1-PCM1 pathway and is altered in Huntington disease. *J. Clin. Invest.* **121**, 4372–4382.

- Lacoste, A., Berenshteyn, F. and Brivanlou, A. H. (2009). An efficient and reversible transposable system for gene delivery and lineage-specific differentiation in human embryonic stem cells. *Cell Stem Cell* **5**, 332-342.
- Leavitt, B. R., Guttman, J. A., Hodgson, J. G., Kimel, G. H., Singaraja, R., Vogl, A. W. and Hayden, M. R. (2001). Wild-type huntingtin reduces the cellular toxicity of mutant huntingtin in vivo. *Am. J. Hum. Genet.* **68**, 313-324.
- Lo Sardo, V., Zuccato, C., Gaudenzi, G., Vitali, B., Ramos, C., Tartari, M., Myre, M. A., Walker, J. A., Pistocchi, A., Conti, L. et al. (2012). An evolutionary recent neuroepithelial cell adhesion function of huntingtin implicates ADAM10-Ncadherin. *Nat. Neurosci.* **15**, 713-721.
- Lopes, C., Aubert, S., Bourgois-Rocha, F., Barnat, M., Rego, A. C., Deglon, N., Perrier, A. L. and Humbert, S. (2016). Dominant-negative effects of adult-onset huntingtin mutations alter the division of human embryonic stem cells-derived neural cells. *PLoS ONE* **11**, e0148680.
- Lu, X.-H., Mattis, V. B., Wang, N., Al-Ramahi, I., van den Berg, N., Frattantoni, S. A., Waldvogel, H., Greiner, E., Osmand, A., Elzein, K. et al. (2014). Targeting ATM ameliorates mutant Huntingtin toxicity in cell and animal models of Huntington's disease. *Sci. Transl. Med.* **6**, 268ra178.
- Mali, P., Yang, L., Esvelt, K. M., Aach, J., Guell, M., Dicarlo, J. E., Norville, J. E. and Church, G. M. (2013). RNA-Guided human genome engineering via Cas9. *Science* **339**, 823-826.
- Messinger, S. M. and Albertini, D. F. (1991). Centrosome and microtubule dynamics during meiotic progression in the mouse oocyte. *J. Cell. Sci.* **100**, 289-298.
- Mitchell, B. D., Gibbons, B., Allen, L. R., Stella, J. and D'Mello, S. R. (2001). Aberrant apoptosis in the neurological mutant Flathead is associated with defective cytokinesis of neural progenitor cells. *Brain Res. Dev. Brain Res.* **130**, 53-63.
- Molero, A. E., Gokhan, S., Gonzalez, S., Feig, J. L., Alexandre, L. C. and Mehler, M. F. (2009). Impairment of developmental stem cell-mediated striatal neurogenesis and pluripotency genes in a knock-in model of Huntington's disease. *Proc. Natl. Acad. Sci. USA* **106**, 21900-21905.
- Molero, A. E., Arteaga-Bracho, E. E., Chen, C. H., Gulino, M., Winchester, M. L., Pichamoorthy, N., Gokhan, S., Khodakhah, K. and Mehler, M. F. (2016). Selective expression of mutant huntingtin during development recapitulates characteristic features of Huntington's disease. *Proc. Natl. Acad. Sci. USA* **113**, 5736-5741.
- Molina-Calavita, M., Barnat, M., Elias, S., Aparicio, E., Piel, M. and Humbert, S. (2014). Mutant huntingtin affects cortical progenitor cell division and development of the mouse neocortex. *J. Neurosci.* **34**, 10034-10040.
- Muñoz-Sanjuán, I. and Brivanlou, A. H. (2002). Neural induction, the default model and embryonic stem cells. *Nat. Rev. Neurosci.* **3**, 271-280.
- Namba, T. and Huttner, W. B. (2017). Neural progenitor cells and their role in the development and evolutionary expansion of the neocortex. *Wiley Interdiscip. Rev. Dev. Biol.* **6**, e256.
- Nekrasov, E. D., Vigont, V. A., Klyushnikov, S. A., Lebedeva, O. S., Vassina, E. M., Bogomazova, A. N., Chestkov, I. V., Semashko, T. A., Kiseleva, E., Suldina, L. A. et al. (2016). Manifestation of Huntington's disease pathology in human induced pluripotent stem cell-derived neurons. *Mol. Neurodegener.* **11**, 27.
- Nopoulos, P. C., Aylward, E. H., Ross, C. A., Mills, J. A., Langbehn, D. R., Johnson, H. J., Magnotta, V. A., Pierson, R. K., Beglinger, L. J., Nance, M. A. et al. (2011). Smaller intracranial volume in prodromal Huntington's disease: evidence for abnormal neurodevelopment. *Brain* **134**, 137-142.
- Ramocki, M. B. and Zoghbi, H. Y. (2008). Failure of neuronal homeostasis results in common neuropsychiatric phenotypes. *Nature* **455**, 912-918.
- Rosa, A., Spagnoli, F. M. and Brivanlou, A. H. (2009). The miR-430/427/302 family controls mesendodermal fate specification via species-specific target selection. *Dev. Cell* **16**, 517-527.
- Ross, C. A. and Tabrizi, S. J. (2011). Huntington's disease: from molecular pathogenesis to clinical treatment. *Lancet Neurol.* **10**, 83-98.
- Ruzo, A., Ismailoglu, I., Popowski, M., Harembaki, T., Croft, G. F., Deglincerti, A. and Brivanlou, A. H. (2015). Discovery of novel isoforms of huntingtin reveals a new hominid-specific exon. *PLoS ONE* **10**, e0127687.
- Sathasivam, K., Woodman, B., Mahal, A., Bertaux, F., Wanker, E. E., Shima, D. T. and Bates, G. P. (2001). Centrosome disorganization in fibroblast cultures derived from R6/2 Huntington's disease (HD) transgenic mice and HD patients. *Hum. Mol. Genet.* **10**, 2425-2435.
- Shi, Y., Kirwan, P., Smith, J., Robinson, H. P. C. and Livesey, F. J. (2012). Human cerebral cortex development from pluripotent stem cells to functional excitatory synapses. *Nat. Neurosci.* **15**, 477-86, S1.
- Sommer, C., Straehle, C., Kothe, U. and Hamprecht, F. A. (2011). Ilastik: Interactive learning and segmentation toolkit. In *Proceedings Eighth IEEE International Symposium on Biomedical Imaging (ISBI)*, pp 230-233. IEEE.
- Sørensen, S. A., Fenger, K. and Olsen, J. H. (1999). Significantly lower incidence of cancer among patients with Huntington disease: an apoptotic effect of an expanded polyglutamine tract? *Cancer* **86**, 1342-1346.
- Steigemann, P., Wurzenberger, C., Schmitz, M. H. A., Held, M., Guizetti, J., Maar, S. and Gerlich, D. W. (2009). Aurora B-mediated abscission checkpoint protects against tetraploidization. *Cell* **136**, 473-484.
- Wexler, N. S., Young, A. B., Tanzi, R. E., Travers, H., Starosta-Rubinstein, S., Penney, J. B., Snodgrass, S. R., Shoulson, I., Gomez, F. and Ramos Arroyo, M. A. (1987). Homozygotes for Huntington's disease. *Nature* **326**, 194-197.
- White, J. K., Auerbach, W., Duyao, M. P., Vonsattel, J.-P., Gusella, J. F., Joyner, A. L. and MacDonald, M. E. (1997). Huntingtin is required for neurogenesis and is not impaired by the Huntington's disease CAG expansion. *Nat. Genet.* **17**, 404-410.
- Zuccato, C., Valenza, M. and Cattaneo, E. (2010). Molecular mechanisms and potential therapeutic targets in Huntington's disease. *Physiol. Rev.* **90**, 905-981.

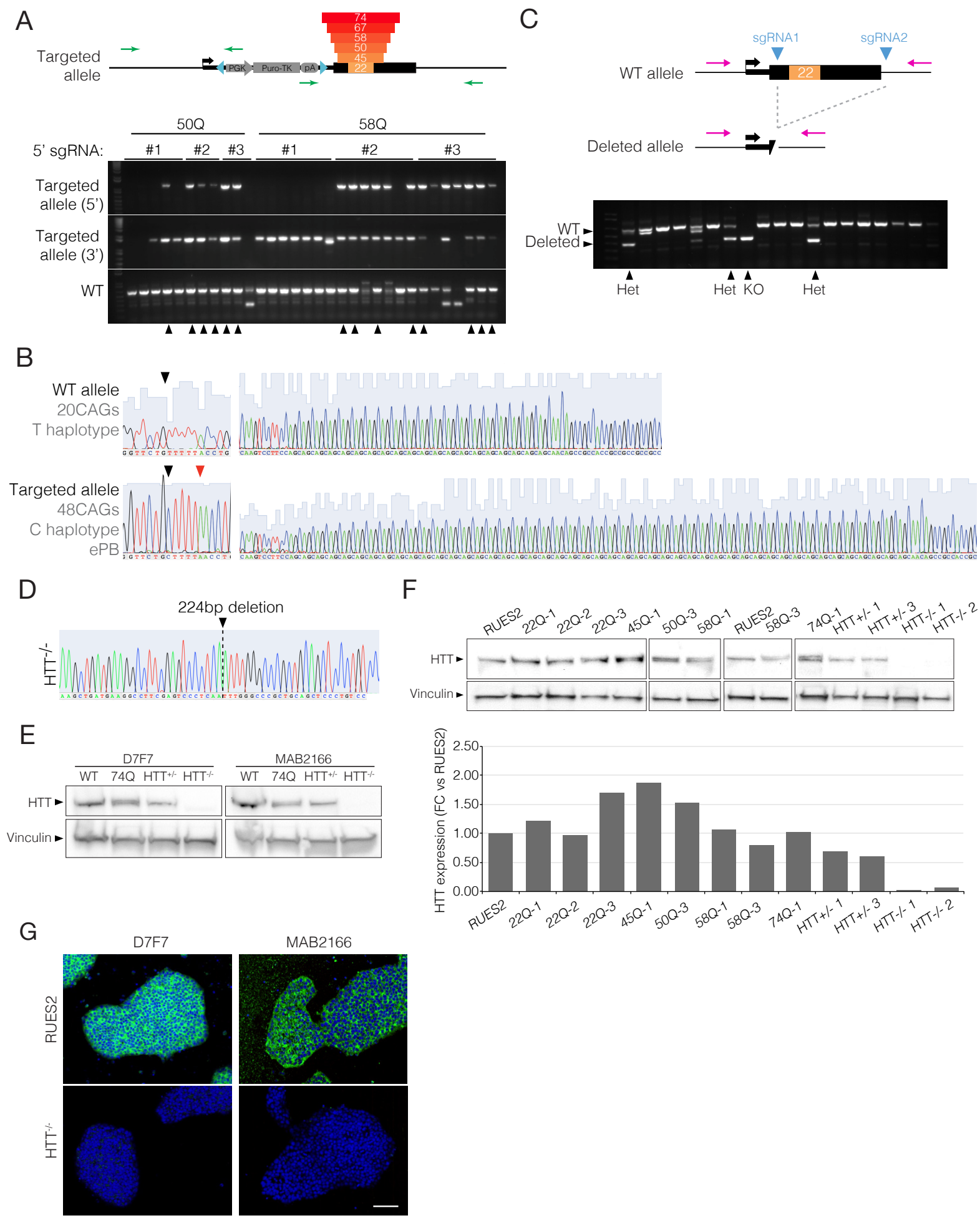


Figure S1. Validation of the HD-hESC allelic series. (A) PCR screening of HD-hESC targeted clones after CRISPR/Cas9-mediated homologous recombination. Primers flanking the 5' and 3' arms were used to detect targeted alleles. A primer pair that amplifies the WT was also used to identify heterozygotically vs homozygotically targeted clones. (B) Sanger sequencing example of both the targeted and untargeted allele in one of the 50Q targeted clones. The convenient location of a heterozygotic SNP allowed for the identification of which of the two alleles was targeted. (C) PCR screening of targeted clones after CRISPR/Cas9-mediated HTT exon 1 deletion. Primers flanking the deleted region were used to detect targeted alleles. (D) Sanger sequencing example of the deleted alleles in a $HTT^{-/-}$ line. (E) Expression of both expanded and wildtype HTT protein is detected in RUES2-74Q, while it is absent in $HTT^{-/-}$ clones and reduced in $HTT^{+/-}$ clones. Western Blot using two independent HTT antibodies: D7F7 and MAB2166. (F) Western Blot using MAB2166 antibody for multiple genotypes and sub-clones, and the appropriate quantification below. HTT expression is variable between genotypes and clones, but consistently decreased at ~60% in the heterozygous clones. (G) Comparison of the HTT subcellular localization in pluripotency conditions by IF using two independent antibodies: D7F7 and MAB2166. Both antibodies provide a cytoplasmic signal, which is clearly excluded from the nucleus. Scale bar 25 μ m.

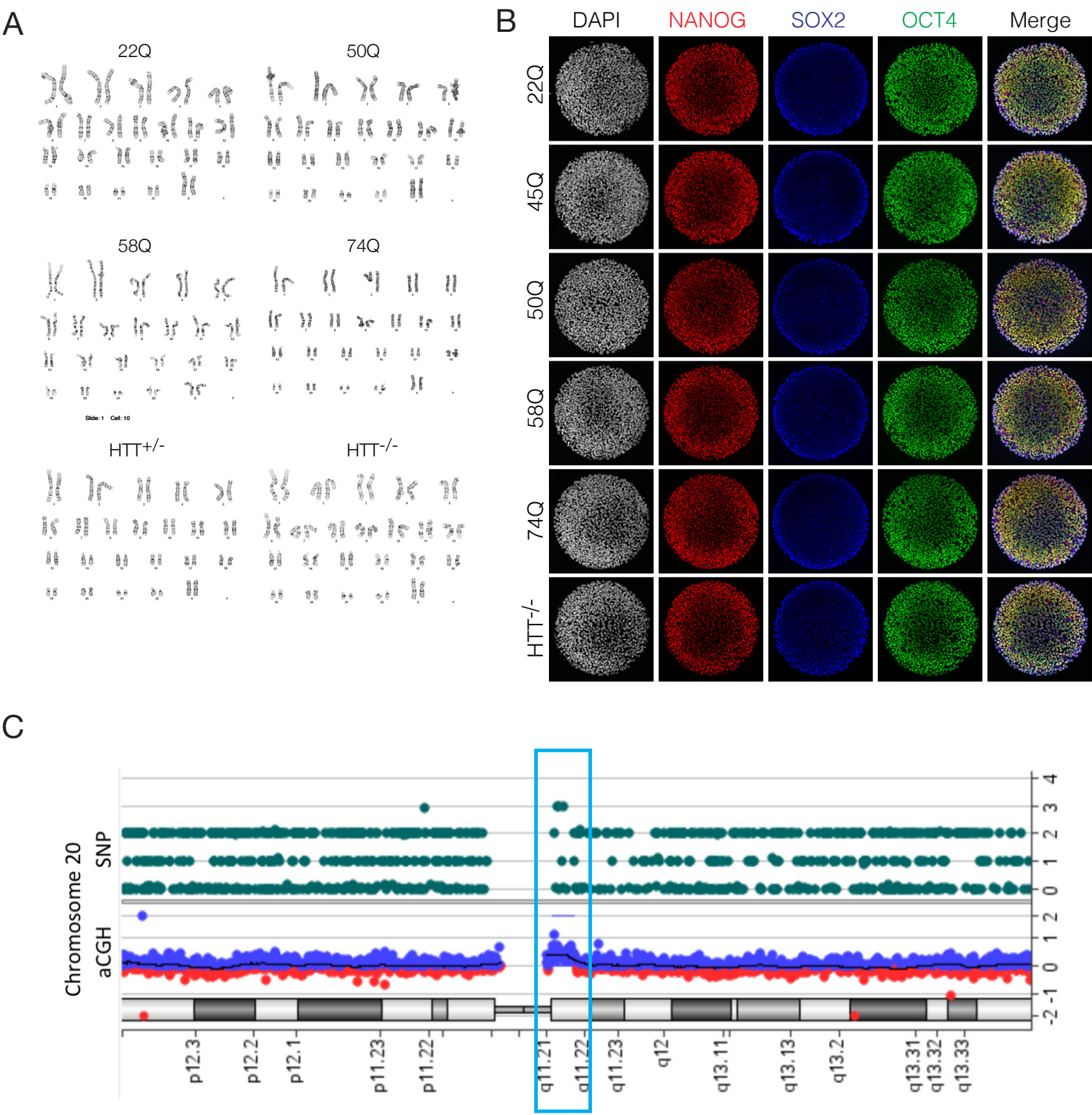


Figure S2. Karyotyping and pluripotency validation of the HD-hESC allelic series

(A) All hESC isogenic clones were karyotypically normal by G-banding. (B) The pluripotency status was not affected by the length of the polyQ tract or the HTT dosage. Immunostaining of micropatterned hESC cultures for pluripotency markers NANOG, SOX2 and OCT4. Scale bar 100µm. (C) Example of aCGH analysis result (amplification of 20q11). aCGH analyses revealed different CNVs present in different sub-clones.

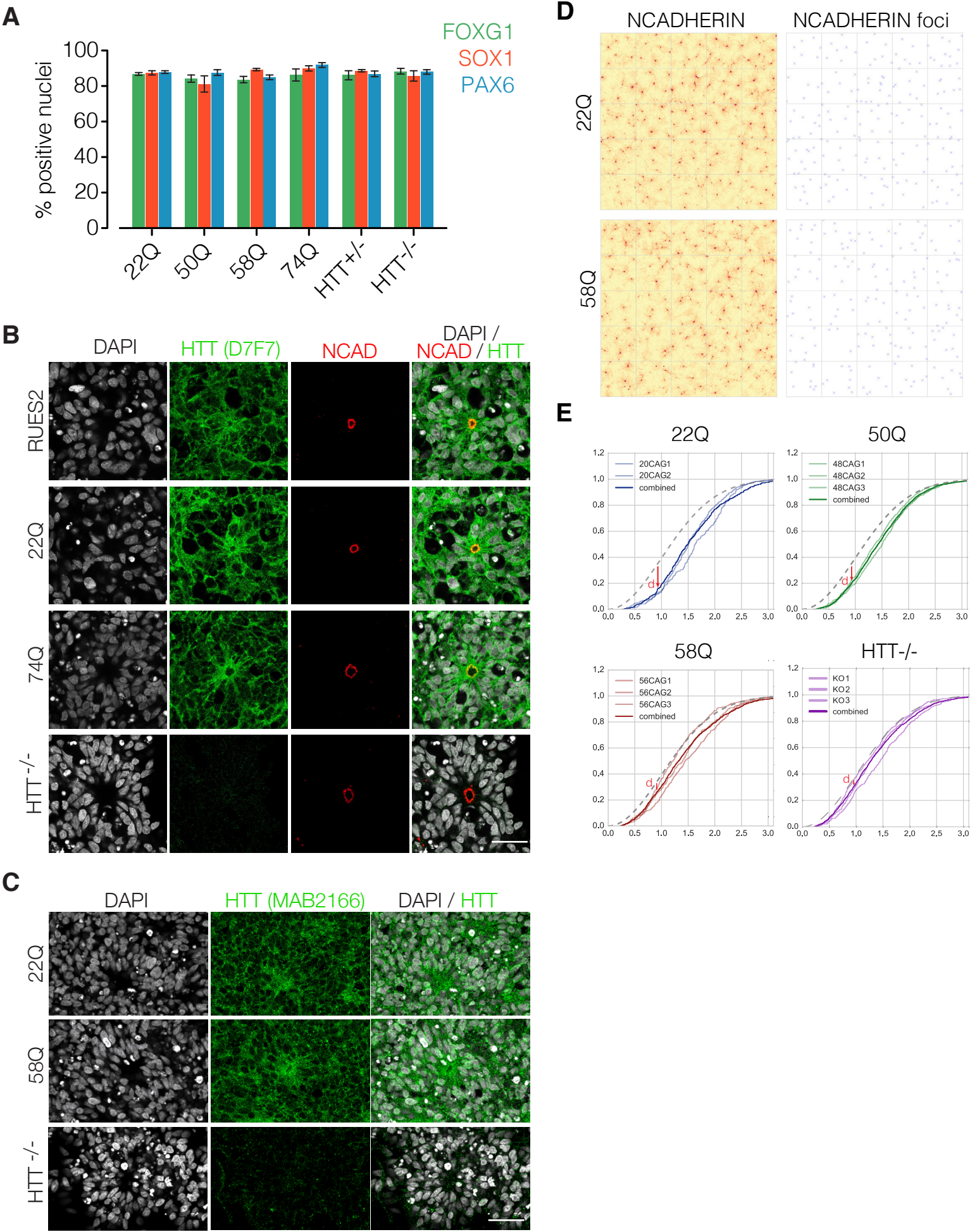


Figure S3. Neural rosette differentiation and impairment of inter-rosette self-organization in expanded polyQ and HTT^{-/-} lines. (A) Neural induction and positional identity were unaffected by polyQ length or HTT dosage. Mean % of all DAPI nuclei positive for SOX1, PAX6, FOXG1, +/- SEM, n=2-3 lines/genotype, >2000 cells scored per line. (B) Full-length HTT protein localized to the cytoplasm in neural progenitors at neural rosette stage and its intracellular localization is not affected by the increasing polyQ lengths. Immunostaining for DNA (DAPI, white), HTT (D7F7, green), and NCADHERIN (red), 40x confocal z-section, Scale Bar 50µm. (C) Immunostaining for DNA (DAPI, white) and HTT (MAB2166, green) in neural progenitors at neural rosette stage, confirming the HTT subcellular localization detected with D7F7 antibody. (D) Representative immunostainings of NCAD foci for 22Q and 58Q lines, and their corresponding locations after image processing. (E) Cumulative distributions of the nearest neighbor distances of individual lines, and combined, compared to the one expected from a random arrangement of rosettes (black dashed line).

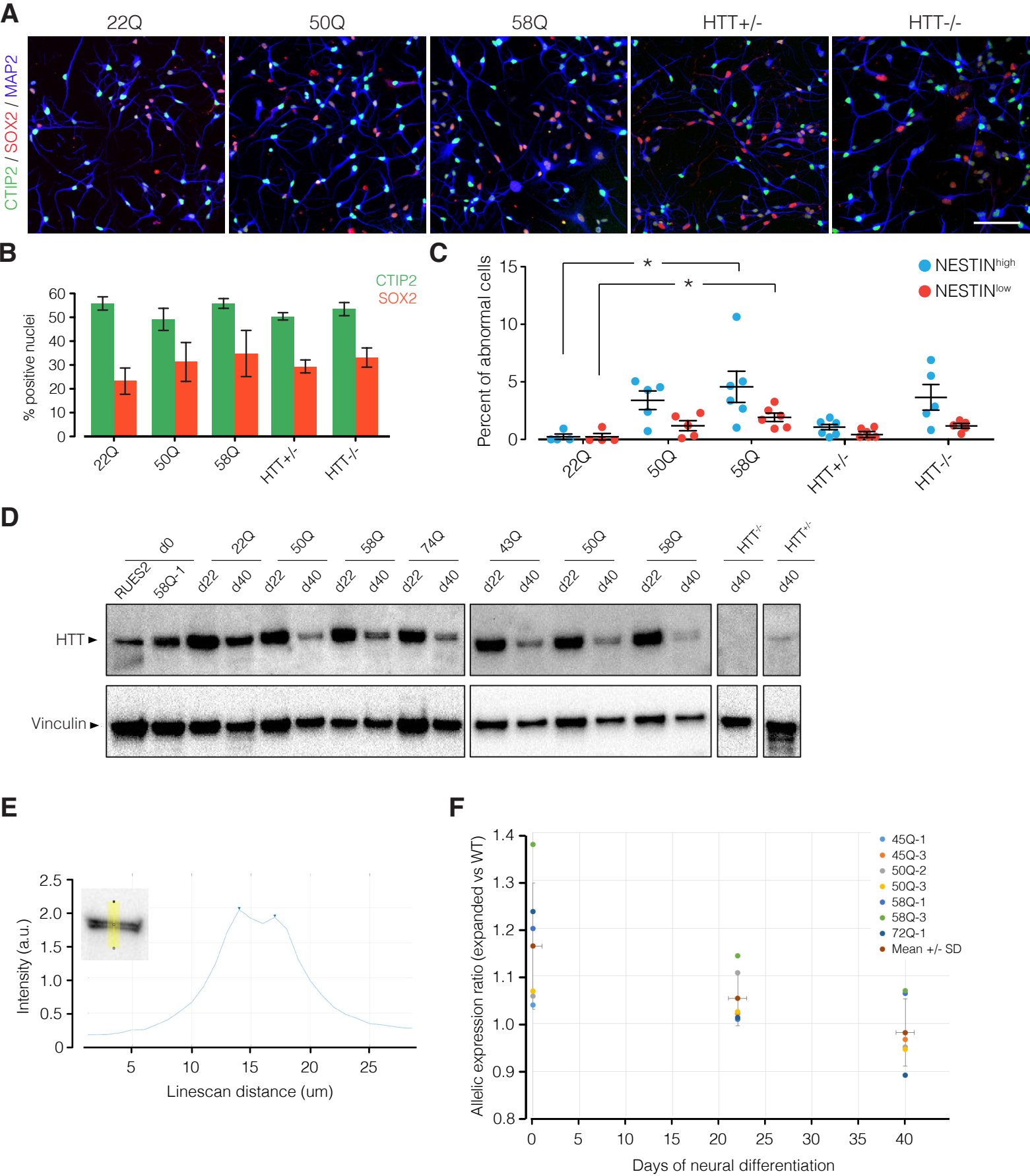


Figure S4. Isogenic HD hESC lines are able to differentiate to post-mitotic neurons, but display morphological phenotypes. (A-B) At day 45, cultures are composed of post-mitotic neurons (A) staining for (MAP2⁺, blue) and cortical neuronal marker CTIP2, and SOX2+ (red) NESTIN⁺ (not shown) progenitor cells, 20x confocal z stack maximum intensity projection with (B) no significant difference in abundance between genotypes. Mean % of DAPI +/- SEM of n=2-3 independent lines per genotype, >1000 cells scored per line. Scale bar 50um. (C) Quantification of the frequency of abnormal cells, classified by phenotype as progenitors (Nestin^{high}), or post-mitotic neurons (Nestin^{low}). * p-value <0.05 in an ANOVA test. (D-F) HTT⁺ allelic expression analysis along neuronal differentiation. (D) Western Blot of representative clones for multiple genotypes at either day 22 or 40 of neuronal differentiation. (E) Example of the method of quantification of the differential allelic expression. (F) Both the expanded and the wildtype allele were expressed at approximately the same levels (ratio expanded vs wildtype ~ 1.1).

Table S1. Analysis of whole genome sequence data from HD allelic lines. No mutations were observed in any of the lines at any of the predicted off-target loci for any of the sgRNAs used in the generation of the lines.

Sample	# of SNP variants in whole genome (compared to hg19)	# of new SNP Variants in whole genome (compared to RUES2)	# of unique new SNP Variants in whole genome (compared to rest of lines)	# <i>de novo</i> Variants near predicted sgRNA25 off-targets	# <i>de novo</i> Variants near predicted sgRNA14 off-targets	# <i>de novo</i> Variants near predicted sgRNA22 off-targets
RUES2 (parental)	4,405,573	N/A	N/A	N/A	N/A	N/A
22Q-1	4,401,985	1,364	1,256	0	0	0
50Q-1	4,416,582	1,491	1,203	0	0	0
50Q-2	4,417,218	2,063	1,934	0	0	0
50Q-3	4,416,294	1,737	1,608	0	0	0
58Q-1	4,413,149	1,346	1,047	0	0	0
58Q-2	4,419,108	1,601	1,394	0	0	0
58Q-3	4,417,117	1,311	1,005	0	0	0
HTT+/- 1	4,416,777	1,376	1,215	0	0	0
HTT+/- 2	4,416,560	958	656	0	0	0
HTT+/- 3	4,402,404	733	466	0	0	0
HTT-/- 1	4,417,789	1,185	893	0	0	0

Table S2. Summary of Arrayed Comparative Genomic Hybridization (aCGH) analysis to assess copy number variations in the RUES2-HD allelic series. We found a variety of copy number variations and loss-of-heterozygosity, within and outside of normal ranges, but these did not correlate with any of the observed phenotypic differences.

Color Legend	Cell line	1	2	3	4	5	6	7	8	9	10	11	12	13	14	15	16	17	18	19	20	21	22	X
AMP	22Q-1		p12 - p11.2 q13 q34		p16.3						q23.32									q13.2-q13.31	q11.21			
DEL	22Q-2		p12 - p11.2 q13		p16.3	q21.3 - q22.1					q23.32				q32.33				q22.1 - q23	q13.2-q13.31				
LOH	22Q-3		p12 - p11.2 q13		p16.3	q21.3 - q22.1		q36.2			q23.32							q12 - q21.31		q13.2-q13.31	q11.21			
	45Q-1		p12 - p11.2 q13			q21.3 - q22.1					q23.32							q12 - q21.31		q13.2-q13.31				
	50Q-1		p12 - p11.2 q13 q14.2		p16.3	q21.3 - q22.1					q23.32				q32.33			q12 - q21.31						
	50Q-2		p12 - p11.2 q13			q21.3 - q22.1					q23.32				q32.33			q12 - q21.31						
	50Q-3		p12 - p11.2 q13		p16.3	q21.3 - q22.1					q23.32		q12.3							q13.2-q13.31				
	58Q-1		p12 - p11.2 q13		p16.3	q21.3 - q22.1					q23.32					q11.1 - q11.2							q22.1-q22.2	
	58Q-2		p12 - p11.2 q13		p16.3	q21.3 - q22.1		q12.1-p11.2			q23.32				q32.33					q13.2-q13.31				
	58Q-3		p12 - p11.2 q13		p16.3	q21.3 - q22.1					q23.32				q32.33			q12 - q21.31		q13.2-q13.31			q22.1-q22.2	
	67Q-1		p12 - p11.2 q13		p16.3	q21.3 - q22.1		q31.32			q23.32				q32.33					q13.2-q13.31				
	74Q-1		p12 - p11.2 q13		p16.3	q21.3 - q22.1					q23.32				q32.33					q13.2-q13.31	q11.21			
	74Q-2		p12 - p11.2 q13 q34		p16.3	q21.3 - q22.1	q22.31				q23.32				q32.33			q12 - q21.31		q13.2-q13.31	q11.21			
	HTT+/- 1		p12 - p11.2 q13		p16.3	q21.3 - q22.1					q23.32				q32.33			q12 - q21.31		q13.2-q13.31			q22.1-q22.2	
	HTT+/- 2		p12 - p11.2 q13		p16.3	q21.3 - q22.1		q31.32			q23.32				q32.33			q12 - q21.31		q13.2-q13.31			q22.1-q22.2	
	HTT+/- 3		p12 - p11.2 q13		p16.3	q21.3 - q22.1					q23.32										q11.21			
	HTT-/- 1		q13		p16.3	q21.3 - q22.1					q23.32				q32.33						q11.21			
	HTT-/- 2		p12 - p11.2 q13		p16.3	q21.3 - q22.1				q33.1	q23.32							q12 - q21.31			q11.21			
	HTT-/- 3		p12 - p11.2 q13		p16.3	q21.3 - q22.1					q23.32				q32.33			q12 - q21.31			q11.21			
	RUES2 parental stock 1		p12 - p11.2 q13		p16.3	q21.3 - q22.1					q23.32				q32.32			q12 - q21.31		q13.2-q13.31				
	RUES2 parental stock 2		p12 - p11.2 q13		p16.3	q21.3 - q22.1					q23.32				q32.33					q13.2-q13.31				
	RUES2 parental stock 3		p12 - p11.2 q13		p16.3	q21.3 - q22.1					q23.32							q12 - q21.31		q13.2-q13.31				

Table S3. Primers

Fragment	Fw primer sequence	Rv primer sequence	Template
pUC57-Kan bb	CTCCAGCTTTTGTTCCTT T	CCAATTCGCCCTATAGTGA GTC	pUC57-Kan plasmid
Left homology arm	AAAGGGAACAAAAGCTG GAGgggtcacacttgggtcct	TCTAGGGTTAAaagcagaacctga gcggc	gDNA from RUES2 (WT)
ePB-PUTK	aggttctgcttTTAACCCTAGAA AGATAGTCTGC	GGGCCGCAGGTTAACCCTA GAAAGATAATCATATTG	ePB-CAG-PUTK-pA plasmid
Right homology arm	TTTCTAGGGTTAACCTGC GGCCCAGAGCCC	GACTCACTATAGGGCGAAT TGGCCTCCCCATCAGCAAC GTGT	gDNA from RUES2 (WT)

Table S4. Templates used for each CAG length.

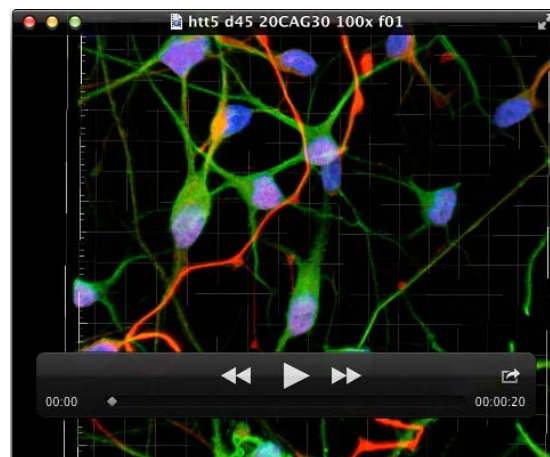
polyQ length	Origin of genomic DNA template	Obtained from
44	ND38548 iPSC	Coriell Biorepository
50	GENEA20 hESC	GENEA
58	QS-001 fibroblasts	Tabrizi lab
69	QS-004 fibroblasts	Tabrizi lab
75	QS-004 fibroblasts	Tabrizi lab

Table S5. sgRNAs

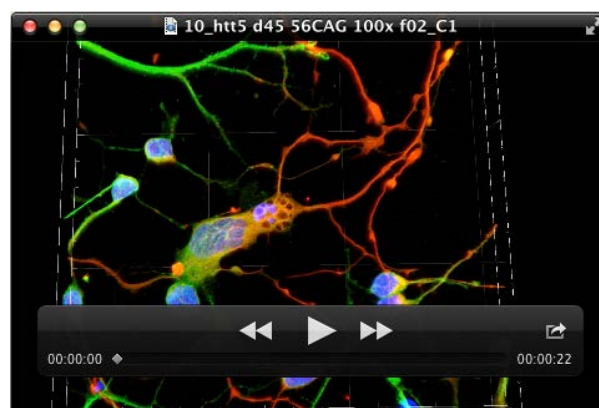
sgRNA	Protospacer + PAM sequence
hHTT_sgRNA25	GGTAAAAGCAGAACCTGAG CGG
hHTT_sgRNA22	CTGCTGCTGGAAGGACTTGA GGG
hHTT_sgRNA14	GCTGCACCGACCGTGAGTTT GGG

Table S6. Antibodies

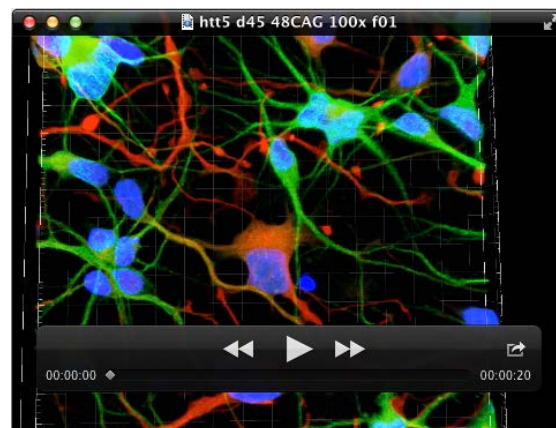
Name	Supplier	Catalog number	Dilution Factor
PAX6	Covance	PRB-278	200
PAX6	BD Biosciences	561462	200
SOX1	R&D	AF3369	1000
NES	EMD Millipore	ABD69	500
FOXG1	Abcam	ab18259	200
HTT (D7F7)	Cell Signaling	5656S	100
N-cadherin	BioLegend	350802	100
Acetylated tubulin	Sigma-Aldrich	T-6793	200
Pericentrin	Abcam	ab28144	200
SOX2	R&D	AF2018	1000
CTIP2	Abcam	ab18465	200
MAP2	Abcam	ab5392	5000
Aurora b kinase	Abcam	ab2254	100
Alpha-tubulin	Abcam	ab89984	500
CREST	Antibodies Incorporated	15-235-0001	100



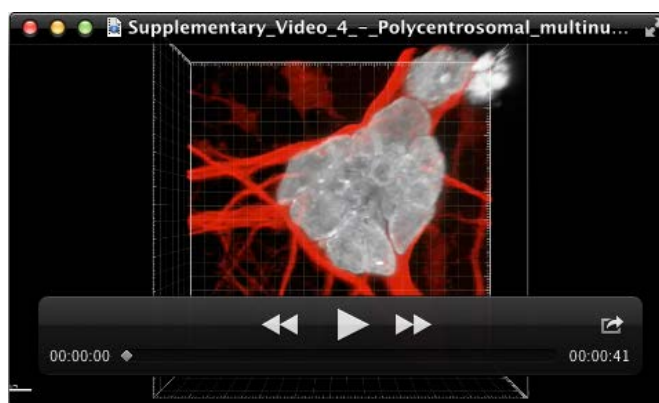
Movie 1. Three-dimensional Imaris rendering of deconvolved 100x confocal z-stack of a normal day 45 neuronal culture of RUES2-22Q stained for MAP2 (green), CTIP2 (purple), nestin (red), and DAPI (blue). Note the thin processes, and the absence of multi-nucleated cells.



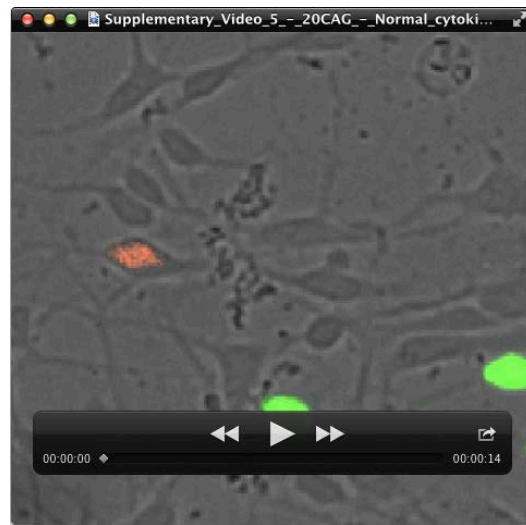
Movie 2. Three-dimensional rendering of 100x confocal z-stack of an abnormal progenitor cell in RUES2-58Q cultures after 45 days of neuronal differentiation, stained for MAP2 (green), CTIP2 (purple), nestin (red), and DAPI (blue). Note the abnormal progenitor cell in the center with an enlarged soma, displaying multiple separated nuclei, thicker processes, enlarged vacuoles and a co-expression of nestin and MAP2 markers.



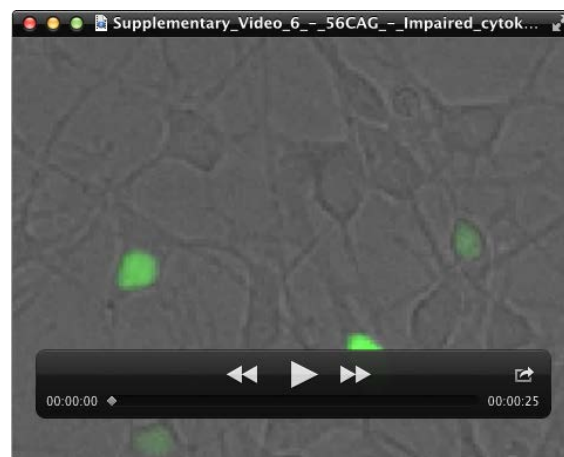
Movie 3. Three-dimensional rendering of 100x confocal z-stack of abnormal post-mitotic neurons in RUES2-50Q cultures after 45 days of neuronal differentiation, stained for MAP2 (green), CTIP2 (purple), nestin (red), and DAPI (blue). Several multinucleated cells can be observed in the region, but of upmost interest is the cell in the top-right, which displays the typical phenotype of abnormal post-mitotic neurons: multiple nuclei linked together by strands of DNA, forming a ‘nuclear bouquet’.



Movie 4. Three-dimensional rendering of 100x confocal z-stack of an abnormal post-mitotic neuron, showing typical nuclear bouquets containing multiple concentric centrosomes located close to the center of the nuclear bouquet, suggestive of strong polarity defects. Adjusted signal for all channels, acetylated tubulin (red), pericentrin (green) and DAPI (white) are shown, followed by surfaces-modeled by thresholding on intensity for DAPI and pericentrin.



Movie 5. Time-lapse imaging of mixed RFP- and GFP-labeled RUES2-22Q cultures between days 28-31 of neuronal differentiation. Note two GFP-labeled daughter cells separate and move independently shortly after cell division.



Movie 6. Time-lapse imaging of mixed RFP- and GFP-labeled RUES2-58Q cultures between days 28-31 of neuronal differentiation. Note two GFP-labeled daughter cells are unable to separate after cell division, and they come back together generating a multinucleated cell.



Movie 7. Time-lapse imaging of mixed RFP- and GFP-labeled RUES2-22Q cultures between days 28-31 of neuronal differentiation. Impaired cell divisions were observed in multiple consecutive rounds of karyokinesis, suggesting that once a multinucleated cell is generated, it cannot be resolved in successive cell divisions.



Movie 8. Three-dimensional rendering of an 100x confocal z-stack of a dividing cell with normal centromere counts (92) displaying lagging chromosomes in RUES2-58Q. DAPI, white; alpha-tubulin, red; CREST (centromere protein reactive serum), green. Scale bar, 5 μ m.